Systems/Circuits

Coupling of Mouse Olfactory Bulb Projection Neurons to Fluctuating Odor Pulses

Debanjan Dasgupta,[1,2] Tom P. A. Warner,[1] Andrew Erskine,[1] and Andreas T. Schaefer[1,2]
[1]Sensory Circuits and Neurotechnology Laboratory, Francis Crick Institute, London NW1 1AT, United Kingdom, and [2]Department of Neuroscience, Physiology and Pharmacology, University College London, London WC1E 6BT, United Kingdom

Odors are transported by turbulent air currents, creating complex temporal fluctuations in odor concentration that provide a potentially informative stimulus dimension. We have shown that mice are able to discriminate odor stimuli based on their temporal structure, indicating that information contained in the temporal structure of odor plumes can be extracted by the mouse olfactory system. Here, using *in vivo* extracellular and intracellular electrophysiological recordings, we show that mitral cells (MCs) and tufted cells (TCs) of the male C57BL/6 mouse olfactory bulb can encode the dominant temporal frequencies present in odor stimuli up to at least 20 Hz. A substantial population of cell-odor pairs showed significant coupling of their subthreshold membrane potential with the odor stimulus at both 2 Hz (29/70) and the suprasniff frequency 20 Hz (24/70). Furthermore, mitral/tufted cells (M/TCs) show differential coupling of their membrane potential to odor concentration fluctuations with tufted cells coupling more strongly for the 20 Hz stimulation. Frequency coupling was always observed to be invariant to odor identity, and M/TCs that coupled well to a mixture also coupled to at least one of the components of the mixture. Interestingly, pharmacological blocking of the inhibitory circuitry strongly modulated frequency coupling of cell-odor pairs at both 2 Hz (10/15) and 20 Hz (9/15). These results provide insight into how both cellular and circuit properties contribute to the encoding of temporal odor features in the mouse olfactory bulb.

Key words: **frequency coupling; *in vivo* electrophysiology; inhibition; olfaction; olfactory bulb; temporal structure in odor**

Significance Statement

Odors in the natural environment have a strong temporal structure that can be extracted and used by mice in their behavior. Here, using *in vivo* extracellular and intracellular electrophysiological techniques, we show that the projection neurons in the olfactory bulb can encode and couple to the dominant frequency present in an odor stimulus. Furthermore, frequency coupling was observed to be differential between mitral and tufted cells and was odor invariant but strongly modulated by local inhibitory circuits. In summary, this study provides insight into how both cellular and circuit properties modulate encoding of odor temporal features in the mouse olfactory bulb.

Introduction

Temporal structure has long been considered an integral part of sensory stimuli, notably in vision (Buracas et al., 1998; Kauffmann et al., 2014, 2015; Borghuis et al., 2019; Chou et al., 2019; Wang et al., 2019) and audition (Nelken et al., 1999; Theunissen and Elie, 2014; VanRullen et al., 2014; Deneux et al., 2016). Odors in natural environments are transported by turbulent air streams, resulting in complex spatiotemporal odor distributions and rapid concentration fluctuations (Shraiman and Siggia, 2000; Celani et al., 2014; Pannunzi and Nowotny, 2019; Marin et al., 2021; Crimaldi et al., 2022). The neuronal circuitry of the olfactory system, particularly in invertebrates, has been shown to support the encoding of temporal structures present in odor stimuli (Hendrichs et al., 1994; Vickers and Baker, 1994; Vickers et al., 2001; Szyszka et al., 2014; Huston et al., 2015; Pannunzi and Nowotny, 2019). Temporal features in odor stimuli such as differences in stimulus onset were shown to be detectable on a behavioral level by bees (Szyszka et al., 2012; Sehdev et al., 2019).

Received July 11, 2021; revised Mar. 24, 2022; accepted Mar. 29, 2022.

Author contributions: D.D. and A.T.S. designed research; D.D. and T.P.A.W. performed research; A.E. contributed unpublished reagents/analytic tools; D.D. and T.P.A.W. analyzed data; D.D. and A.T.S. wrote the paper.

This work was supported by the Francis Crick Institute, which receives its core funding from Cancer Research United Kingdom (UK; Grant FC001153); the UK Medical Research Council (Grant FC001153); the Wellcome Trust (Grant FC001153); the UK Medical Research Council (Grant reference MC_UP_1202/5); Wellcome Trust Investigator Grant 110174/Z/15/Z (to A.T.S.); and the National Science Foundation/Canadian Institutes of Health Research/German Research Foundation/ Fonds de Recherche du Québec/UK Research and Innovation–Medical Research Council Next Generation Networks for Neuroscience Program (Award No. 2014217). We thank the animal facilities at the National Institute for Medical Research and the Francis Crick Institute for animal care and technical assistance, the mechanical and electronic workshop (Alan Ling, Adam Hurst, Martyn Stopps), Dr. Swagata Ghatak and members of the Sensory Circuits and Neurotechnology Laboratory for comments on earlier versions of the manuscript, and Dr. Rebecca Jordan for help during the initial days of whole-cell recordings.

The authors declare no competing financial interests.

Correspondence should be addressed to Debanjan Dasgupta at d.dasgupta@ucl.ac.uk or Andreas T. Schaefer at Andreas.Schaefer@crick.ac.uk.

https://doi.org/10.1523/JNEUROSCI.1422-21.2022

In mammals, reports have indicated that the neural circuitry of the early olfactory system readily sustains temporally modulated and precise action potential discharge (Cury and Uchida, 2010; Shusterman et al., 2011; Gupta et al., 2015) and is able to relay information about optogenetic stimuli with ~10 ms precision (Smear et al., 2011; Li et al., 2014; Rebello et al., 2014). Furthermore, we have recently shown that mice can use information in the temporal structure of odor stimuli at frequencies as high as 40 Hz to guide behavioral decisions (Ackels et al., 2021).

The olfactory bulb (OB) is the first stage of olfactory processing in the mammalian brain. Olfactory sensory neurons (OSNs) in the nasal epithelium convert volatile chemical signals into electrical activity forming the input to the OB. Air flow through the nasal cavity, transport of odors through the mucus, and the multistep biochemical signal transduction together result in slow odor responses in OSNs (Sicard, 1986; Reisert and Matthews, 2001), creating the general notion that mammalian olfaction has a limited temporal bandwidth. Although OSN activity indeed reflects a low-pass filtered version of the incoming odor signal (Verhagen et al., 2007), information about different frequency components can still be present in OSN population activity (Nagel and Wilson, 2011). Moreover, circuit mechanisms in other brain regions and species have been shown to boost high-frequency content and sharpen stimulus presentation (Tramo et al., 2002; Atallah and Scanziani, 2009; Nagel et al., 2015; O'Sullivan et al., 2019). Given the intricate circuitry present in the OB, where multiple types of interneurons process incoming signals (Aungst et al., 2003; Fukunaga et al., 2012; Kato et al., 2013; Miyamichi et al., 2013; Fukunaga et al., 2014; Banerjee et al., 2015; Burton, 2017), we decided to investigate whether the OB circuitry plays a role in representing and processing the temporal features of odor stimuli.

Here, we show that mitral cells (MCs) and tufted cells (TCs), the OB output neurons, respond to odors, temporally modulated at frequencies of 2–20 Hz, in a frequency-dependent manner. Using whole-cell recordings, we show that subthreshold mitral/tufted cell (M/TC) activity *in vivo* can follow odor frequencies both at sniff and suprasniff range for monomolecular odors and odor mixtures. We observe that although putative tufted cells (pTCs) and putative mitral cells (pMCs) show similar frequency coupling capacity at 2 Hz, tufted cells have a higher propensity to follow odor frequencies at 20 Hz. Pharmacologically clamping GABA receptors (Fukunaga et al., 2012) we show that local inhibition in the OB strongly modulates frequency coupling of M/TCs.

Materials and Methods

Experimental design

All the experiments were performed using 5- to 8-week-old C57BL6 male animals. For the unit recordings a NeuroNexus Poly3 probe was used, and for the whole-cell recordings standard borosilicate glass pipettes were used (described below). The odor stimulation was performed using a custom-built temporal olfactory delivery device (tODD) run by custom written software in python. The details of the tODD are described below.

Animals

All animal procedures performed in this study were approved by the United Kingdom government (Home Office) and by the Institutional Animal Welfare Ethical Review Panel. Five- to 8-week-old C57/Bl6 males were used for the study. The study involved six animals for the extracellular unit recordings and 25 animals for the whole-cell patch recordings. The mice were housed up to five per cage under a 12/12 h light/dark cycle with *ad libitum* food and water.

Reagents

All odors were obtained at the highest purity available from Sigma-Aldrich. Unless otherwise specified, odors were diluted 1:5 with mineral oil in 15 ml glass vials (27162 (vials); 27163 (screw caps), Sigma-Aldrich).

High-speed odor delivery device

A high speed odor delivery device was built as described previously (Ackels et al., 2021). Briefly, we connected four VHS valves (catalog #INKX0514750A, Lee) to odor containing 15 ml glass vials (27162, Sigma-Aldrich) through individual output filters (catalog #INMX0350000A, Lee). The vials were connected to a clean air supply (1 L/min) through individual input flow controllers (catalog #AS1211F-M5-04, SMC Pneumatics). Each valve was controlled through a data acquisition module (National Instruments) controlled by a custom-written script using Python software (PyPulse, PulseBoy; https://github.com/warnerwarner).

In vivo *electrophysiology*

Surgical and experimental procedures. Before surgery, all surfaces and apparatus used were sterilized with 1% trigene. Five- to 8-week-old C57BL/6Jax mice were anesthetized using a mixture of ketamine/xylazine (100 mg/kg and 10 mg/kg, respectively) by intraperitoneal injection. Depth of anesthesia was monitored throughout the procedure by testing the toe-pinch reflex. The fur over the skull and at the base of the neck was shaved away and the skin cleaned with 1% chlorhexidine scrub. Mice were then placed on a thermoregulator (DC Temperature Controller, FHC) heat pad that was controlled using feedback from a thermometer inserted rectally. While the animal was on the heat pad, the head was held in place with a set of ear bars. The scalp was incised and pulled away from the skull with 2 arterial clamps on each side of the incision. A custom head-fixation implant was attached to the base of the skull with medical super glue (Vetbond, 3M) so that its most anterior point rested ~0.5 mm posterior to the bregma line. Dental cement (Paladur, Heraeus Kulzer; Simplex Rapid Liquid, Associated Dental Products) was then applied around the edges of the implant to ensure firm adhesion to the skull. A craniotomy over the right olfactory bulb (~2 mm diameter) was made with a dental drill (Success 40, Osada) and then immersed in artificial CSF (ACSF) containing the following (in mM): 125 NaCl, 5 KCl, 10 HEPES, pH adjusted to 7.4 with NaOH, 2 $MgSO_4.7H_2O$, 2 $CaCl_2.2H_2O$, 10 glucose, before removing the skull with forceps. The dura was then peeled off using a bent 30 gauge needle tip.

Following surgery, mice were transferred to a custom head-fixation apparatus with a heat-pad (RS Components) connected to a DC Temperature Controller (FHC). The animals were maintained at 37 ± 0.5°C.

Unit recording. A NeuroNexus Poly3 probe was positioned above the OB craniotomy. An Ag/Ag^+Cl^- reference coil was immersed in a well that was constructed of dental cement around the craniotomy. The reference wire was connected to both the ground and the reference of the amplifier board (catalog #RHD2132, Intan Technologies), which was connected (connector from Omnetics) to a head-stage adapter (catalog #A32-OM32, NeuroNexus). The probe, after zeroed at the OB surface, was advanced vertically into the dorsal OB at <4 μm/s. This was continued until the deepest channels showed a decrease in their recorded spikes, indicating the end of the dorsal mitral cell layer. This was largely in the range of 400 to 600 μm from the brain surface. The signal from the probe was fed into a OpenEphys acquisition board (https://open-ephys.org/acquisition-system/eux9baf6a5s8tid06hk1mw5aafjdz1) and streamed through the accompanying graphical user interface software (https://open-ephys.org/gui). The data were acquired at 30 kHz and displayed both in a raw format and a bandpass-filtered (300–6 kHz) format. The bandpassed format was used primarily to visualize spikes across channels during the recording.

Odor stimulation (unit recordings). Four odors (ethyl butyrate, 2-hexanone, isoamyl acetate, and eucalyptol) were diluted in mineral oil, as mentioned previously, in a ratio of 1:5.

Temporal structure of the odor stimulation was created using the VHS valves while blank valves helped maintain constant air flow throughout the stimulation period (Fig. 1*B*). The start of a stimulation was always triggered to the start of inhalation, which was continuously monitored online using a flow sensor (catalog #AWM2000, Honeywell). A minimum 8 s intertrial interval was given for all the experiments.

The onset pulse was passed to the OpenEphys acquisition board so that the trial trigger was recorded simultaneously with the neural data. A total of 800 trials was presented during the experiment, consisting of 32 repeats of five different frequencies for four odors and one blank. Each trial lasted 2 s and was spaced a minimum of 8 s between the offset of one trial and the onset of the following trial.

Whole-cell recording. Borosilicate pipettes (2 × 1.5 mm) were pulled and filled with the following (in mM): 130 $KMeSO_3$, 10 HEPES, 7 KCl, 2 ATP-Na_2, 2 ATP-Mg, 0.5 GTP-Na_x, 0.05 EGTA, pH 7.3, osmolarity ~290 mOsm/kg. The OB surface was submerged with ACSF containing the following (in mM): 135 NaCl, 5.4 KCl, 5 HEPES, 1 $MgCl_2$, 1.8 $CaCl_2$, pH 7.4, ~300 mOsm/kg. Signals were amplified and low-pass filtered at 10 kHz using an Axoclamp 2B amplifier (Molecular Devices) and digitized at 40 kHz using a Micro 1401 analog-to-digital converter (Cambridge Electronic Design).

After zeroing the pipette tip position at the OB surface, we advanced the tip to reach a depth of ~200 µm from the surface. Next, we stepped at 2 µm/s to hunt for a cell in a similar manner as described before (Margrie et al., 2002; Margrie and Schaefer, 2003; Jordan, 2021). After getting a successful hit, we released the positive pressure to achieve a gigaseal. The next gentle suction helped achieve the whole-cell configuration. We swiftly shifted to current-clamp mode to start a recording. Series resistance was compensated and monitored continuously during recording. Neurons showing series resistance >25 MΩ were discarded from further analysis.

The vertical depths of recorded neurons reported (see Figs. 4*B*, 6*E*,*F*) are vertical distances from the brain surface. Respiration was recorded using a mass flow sensor (catalog #A3100, Honeywell) and digitized at 10 kHz.

The $GABA_A$ clamping experiments were performed as described previously (Fukunaga et al., 2012). Briefly, muscimol and gabazine (Tocris Bioscience) were dissolved in ACSF to achieve a final concentration of 2 mM (muscimol) and 0.4 mM (gabazine). In a subset of experiments, this solution was superfused after ~10 min of recording under control conditions.

Odor stimulation (whole-cell recording). Odors were presented as mixtures of monomolecular odorants mixed in a 1:1 ratio, which was eventually diluted in mineral oil in a 3:7 ratio. Odor A (ethyl butyrate plus 2-hexanone) and B (isopentyl acetate plus eucalyptol) were used for *in vivo* patch-clamp experiments. Odor presentations were triggered on the onset of inhalation of the mouse as described for the unit recordings. The temporal structure of the odor pulses and the triggering of the blank valves were done as for the unit recording experiments described above. A minimum 8 s intertrial interval was given for all the experiments.

Analysis

Fidelity. Fidelity was defined here as the value of peak to trough of each square pulse normalized to the peak to baseline value. A fidelity of 1 therefore indicates that odor fully returns to baseline value between subsequent pulses, whereas a fidelity of ~0 for the flow indicates an almost continuous square pulse of air flow devoid of temporal structure.

Odor-respiration convolution. Photoionization detector (PID) traces were taken of the odor stimuli from the same position as the mice were in during the unit recording experiments. Each frequency was presented four times, with two different odors (ethyl butyrate and isoamyl acetate) randomly presented with 10 s of intertrial interval. This replicated the actual odor presentation to animals. The average signal from the four repetitions were used for the odor-sniff convolution outlined below.

Convolution step. First, the respiration signal was high-pass filtered, flipped, and median subtracted so that the inhalation was now positive and exhalation negative. All values below zero, and therefore any that were linked to the exhalation, were set to zero. Using the find peaks function, the times and heights of the inhalation peaks were recorded. The respiration trace was deemed to be in the inhalation phase when the signal had reached 5% of the total inhalation peak value and was deemed to have reached the end of inhalation when this threshold was reached again after peak.

The PID odor signal was resampled using scipy.signal.resample to have the same sampling frequency as the respiration signal (from 10 kHz up to 30 kHz).

The inhalation-only signal was convolved with the PID signal for the stimuli. Therefore, the resulting odor signal was modulated by the flow rate at any given time point. This convolved signal was then summed over the same time windows as in the binary convolution.

The convolutions were repeated for all presentations during the experiments using the same averaged PID signals. To compare the odor signal among all the frequencies, we applied Mann–Whitney *U* tests to the distributions of total odor calculated. The significance values for these tests were subjected to a Bonferroni correction to account for multiple comparisons.

Single unit responses

Unit responses to blank stimuli were first subtracted from the responses to odor stimuli at the same frequency. These subtracted responses were then averaged across repetitions of the same frequency to produce averaged subtracted cell responses (one per frequency). These responses were then *z*-scored so that they had an average response of zero and an SD of one, with each unit represented by an associated five-value *z*-scored response vector. These *z*-scored responses were clustered using the scipy.cluster.hierarchy.linkage function, which groups units together by the distances between responses in the five-dimensional space they occupy. The output was optimally ordered, ensuring that the global distances between neighboring cells was minimized.

pTC versus pMC classification

We classified our recordings (both unit and whole-cell) into putative tufted cells and putative mitral cells based on the methodology in Fukunaga et al. (2012). We detected the exhalation peaks for every sniff cycle for the baseline period of a given recording, which were then segregated into single sniffs with the corresponding spike-clipped membrane potential (whole cell) or spike (unit recording). The membrane potential was then averaged over all sniff cycles while an average spike probability vector was created from the unit recording. Next, the sniff cycle and the thus obtained membrane potential or spike probability was converted into a phase plot, with phase 0 indicating peak exhalation. Then the preferred phase of the resultant membrane depolarization or spiking probability was detected and considered to be the phase of respiration coupling for the given cell/unit. Next, we classified cells into pTC if the phase of respiration coupling was in the range of 0 to 160° and pMC if in the range of 190 to 350°. Cells that did not have their phase in either of these ranges were not considered in any of the classes.

Spike sorting

Kilosort2 (https://github.com/MouseLand/Kilosort2) was used to spike-sort detected events into clusters. Clusters were then manually curated using phy2 (https://github.com/cortex-lab/phy) and assigned a good, multiunit activity (MUA), or noise label depending on whether they were considered to be made up of neural spikes (good and multiunit activity) or false detections (noise). The clusters made up of spikes were further divided into good or MUA, dependent on whether they are thought to be spikes from a well-isolated single unit. A good unit is characterized by a well-defined rest period in its autocorrelogram, a characteristic spike waveform, and a stable firing rate and spike amplitude (However, these can both vary throughout the recording; Fig. 2*D*–*F*). Only good clusters were used for further analysis.

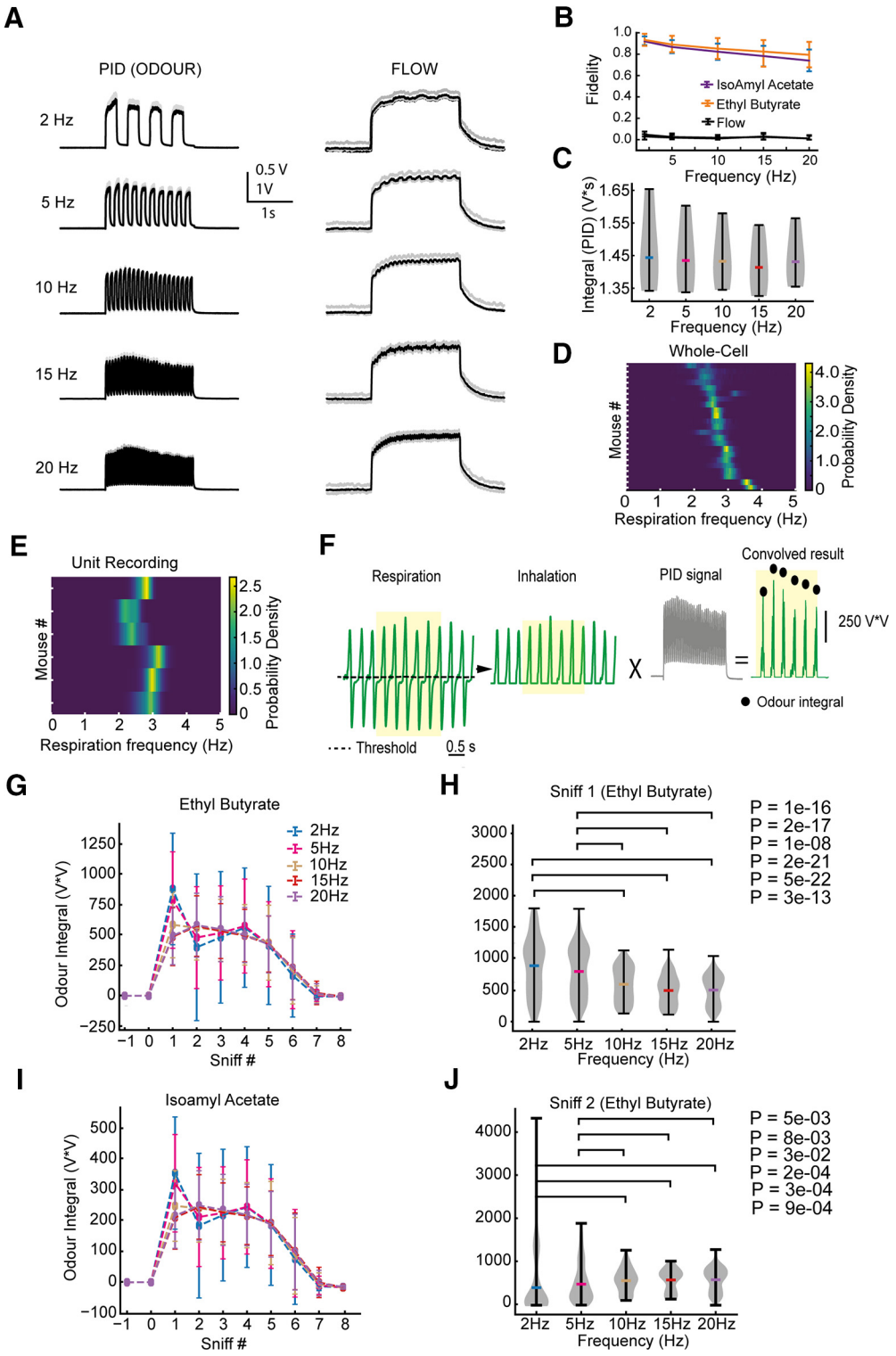

Figure 1. Respiration and odor interaction. ***A***, PID signal (left) and airflow (right) measurements of ethyl butyrate stimuli at five different frequencies. ***B***, Fidelity of the odor stimuli and flow at different frequencies. ***C***, Integral values of the total odor for the five frequencies, shown in ***B***, for 3 s after odor onset (2 s of odor and 1 s to allow full return to baseline). ***D***, Heat map of the probability density of the respiration rate recorded from the animals during the whole-cell recordings ($n = 25$). Each row represents an animal. ***E***, Same as ***D*** but from animals used for the unit recordings ($n = 6$). ***F***, An example outlining the convolution method used to measure the odor signal present in single inhalations. The black dotted line represents the threshold for the start of inhalation. The black filled circles represent the odor integral obtained by convolving the inverted inhalation with the PID signal. ***G***, The odor integral in each inhalation for the entire duration of ethyl butyrate presentation. The filled circles represent mean values obtained from all the animals for a given frequency. The error bars represent the SD. ***H***, Violin plot of the odor integral values in the first sniff after the start of ethyl butyrate presentation. ***I***, Same as in ***G*** but for isoamyl acetate. ***J***, Same as in ***H*** but for sniff 2 for ethyl butyrate presentation.

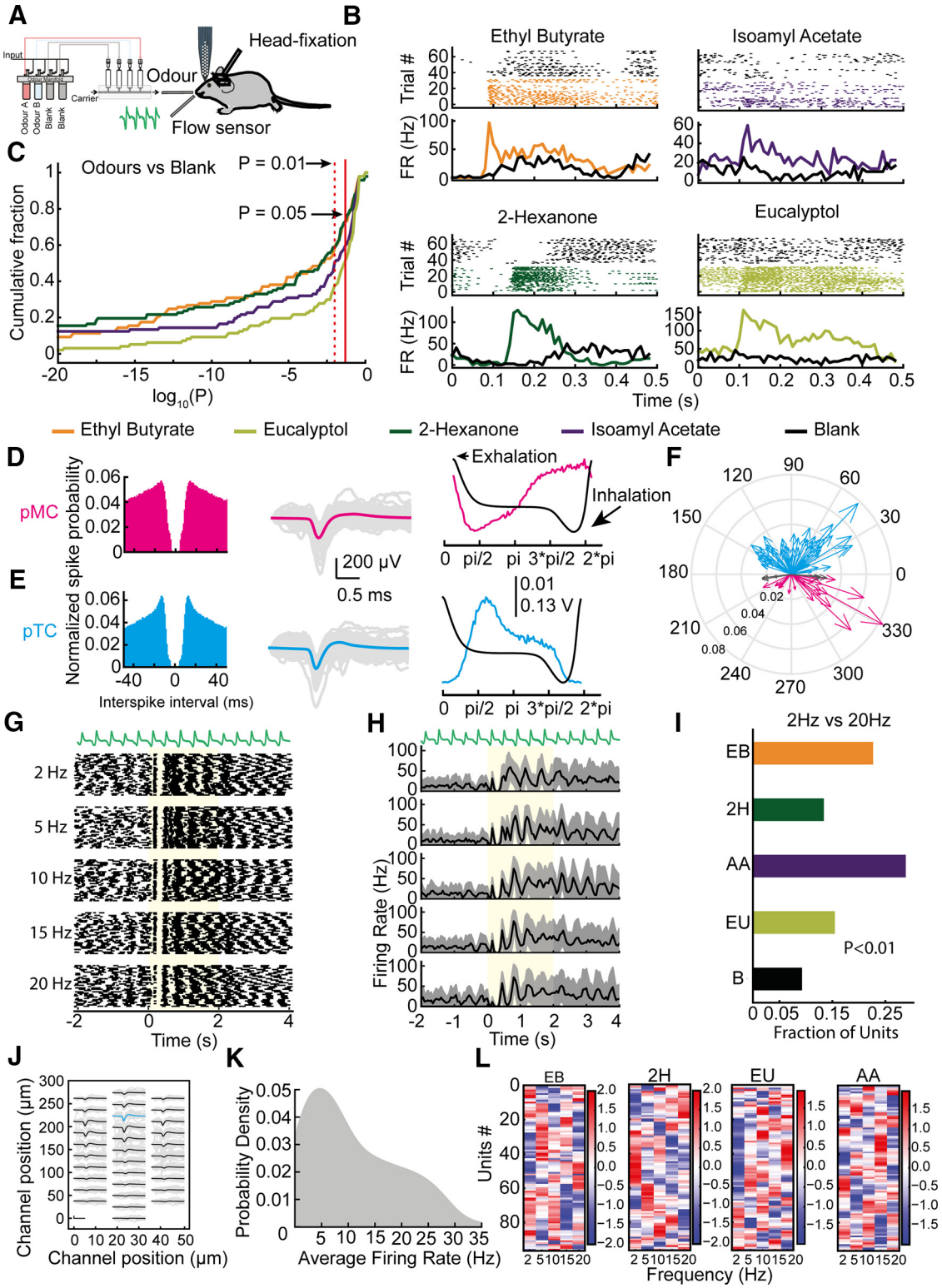

Figure 2. OB neurons encode odor frequency. ***A***, Schema of the unit recording experimental setup. ***B***, Example recordings from single units for the odors and corresponding blank trials. For each odor, the top is the raster and the bottom is the average PSTH. ***C***, Cumulative fraction of units versus Log(*p*) values obtained by comparing the spike times in the first 500 ms after odor onset with that for the blank trials. The *p* values were obtained using Mann–Whitney *U* test. ***D***, Autocorrelogram from a good example pMC (left), individual spike waveforms from the cell (gray), and its average waveform (magenta, middle) and baseline spiking probability (magenta) overlaid on the respiration trace (black, right). Peak spiking probability coincides with inhalation phase of the animal. ***E***, Same as in ***D*** but for putative tufted cell (cyan) with peak firing probability coincides with exhalation phase of the animal. ***F***, Summary phase plot displaying peak firing probability of all recorded units against phase of respiration ($n = 64$; pTC, cyan, $n = 26$; pMC, magenta, and $n = 7$; unresolved, black). ***G***, Respiration trace (top) and raster plot for a response of a single unit to five odor frequencies. ***H***, Respiration trace (top) and average PSTH of the responses of the same unit in ***G***. ***I***, Fraction of units showing significant difference ($p < 0.01$, Mann–Whitney *U* test) in firing rate in the first 500 ms after odor onset between the 2 and 20 Hz odor stimuli. The different colors represent the different odors used for all the units. EB, ethyl butyrate; 2H, 2-hexanone; AA, isoamyl acetate; EU, eucalyptol; S, shuffled. ***J***, Average waveform for the pTC in ***E*** across all channels of recording probe. Average waveforms shown in black, with the cyan average indicating the channel with the largest average waveform. ***K***, Baseline firing rate distribution of all recorded units across all experiments. ***L***, The *z*-scored average change

Linear classifier

Ninety-seven clusters across six animals were grouped and used for classification. Windows used to bin spikes varied both in size and in start relative to odor onset. Window starts span 0 s to 3.99 s from odor onset. The window sizes ranged from 10 ms to 4 s. All classifiers did not consider spikes from >4 s from odor onset. Therefore, a classifier with a 500 ms window range could start between 0 s and 3.5 s, and a window range of 1 s would use starts up to 3 s from odor onset. This full range of starts and widths was used to determine both the time after odor onset that frequencies could be distinguished and the time window required.

The datasets were always of the dimensions 160 × 97, where 160 is the number of trials and 97 the number of clusters. The range of unit responses was scaled to have a mean response of zero and an SD of one. The data were split into a training (80%) and a test set (20%). The training set was used to train a linear support vector machine (SVM) with a low regularization parameter. The low regularization parameter translates to less restrictions in weightings assigned to each cluster by the classifier. Once the classifiers had been trained, they were tested with the remaining 20% of trials. The trials to be saved for testing were picked at random. Training and testing were repeated 1000 times with a random selection of testing trials used each time. Classifiers were then trained on the same data but with their labels shuffled. To test how accuracy varied with the number of clusters, random subsets of clusters were selected and used to train and test the classifiers.

Classifiers were then trained and tested on all one-to-one combinations of trials from the experimental dataset. In this case a classifier was trained on all but two trials, one from each of the two trial types present in the training data. In this set, chance was 50%. Finally, a series of classifiers were trained on all frequencies across all odors, with a single trial from every type being withheld for the test set. As there were 20 total trial types (five frequencies with four odors), chance was 4%.

Single-cell classifier. To test the accuracy of single cells in separating just 2 Hz from 20 Hz, a series of classifiers were trained and tested, in the method outlined above, on single-cell responses to the 2 Hz and 20 Hz stimuli. These classifications were repeated 1000 times with different splits in the StratifiedKFold shuffle. The cells were then ordered from the lowest average classifier accuracy (across the four odors) to the highest classifier accuracy.

Change in membrane potential

The raw recordings were spike clipped using a custom script in spike2 (Cambridge Electronic Design). They were then stored into MATLAB (MathWorks) readable files for further analysis.

All the recordings used were baseline subtracted to rule out the effect of sniff-related background membrane potential oscillations. This was done as described previously (Abraham et al., 2010). Briefly, stretches of baseline period were collated after matching the sniff phase to that during the actual odor presentation. The membrane potential associated with these baseline periods was averaged to make a generic baseline trace for every cell. This was then subtracted from all the recorded traces during the odor stimulation period to create a baseline subtracted trace.

For calculating the average change in membrane potential for 2 and 20 Hz, we averaged the membrane potential in a 2 s period before odor onset (Vm_{base}). Next, we averaged the membrane potential in the first 500 ms (~2 sniffs) after odor onset ($Vm_{odor500}$) and subtracted from the baseline average voltage, in short, as follows:

$$Avg\ .\ change\ in\ membrane\ potential = Vm_{odour500} - Vm_{base}.$$

Change in spike frequency

Action potentials were counted in the raw data and converted into spike frequency in bins of 50 ms. Bar plot of the spike frequency yielded peristimulus time histogram (PSTH) plots (see Fig. 4*E*). Further, we calculated the average spike frequency in 2s before onset (FR_{base}) and 500 ms after onset ($FR_{odor500}$) and eventually subtracted them from each other to calculate the net change in spike frequency, in short, as follows:

$$Avg\ .\ change\ in\ spike\ frequency = FR_{odour500} - FR_{base}.$$

Frequency coupling coefficient estimation

Baseline-subtracted membrane potential traces for every odor and frequency were collected (see Fig. 5*A*, middle). PID traces recorded for the 2 Hz and 20 Hz odor stimulation were averaged over 10 different trials (see Fig. 5*A*, top). Next, we cross-correlated the PID trace and all the individual baseline subtracted traces. This was repeated for all the trials for a given odor and frequency. We selected the peak correlation ($CCodor_{2Hz}$ or $CCodor_{20Hz}$) for all the trials. Similarly, we repeated the same exercise for the control blank stimulus, which was also delivered at 2 and 20 Hz, and obtained a $CCblank_{2Hz}$ or $CCblank_{20Hz}$. Next, we normalized the CCodor with the CCblank for the respective frequencies and averaged them over all the trials to achieve a frequency coupling coefficient (C*p*C) for a given cell-odor pair as follows:

$$CpC = \frac{CCodour_{2Hz}}{CCblank_{2Hz}} \text{ and } CpC = \frac{CCodour_{20Hz}}{CCblank_{20Hz}}.$$

Baseline control CpC

For every recorded cell, we isolated the baseline periods for all the trials. These were then baseline subtracted as described before. Next, we cross-correlated each of these baseline traces with the 2 Hz and 20 Hz PID signals to obtain the peak cross-correlation value. The C*p*C value for all the baseline traces for a given cell were then calculated in the same manner as described above. This set of C*p*C baseline 2 and 20 Hz was then used to determine statistical difference from the C*p*C odor 2 and 20 Hz.

Statistics

When only two groups were compared, a nonparametric Student's *t* test (paired and unpaired) has been used with Bonferroni correction in the case of multiple comparison. When more than two groups were compared, we used one-way ANOVA. Bars and scatter plots are represented with mean ± SD of the population. The box plots are represented with the median (midline), the 25th percentile (top edge), and the 75th percentile (bottom edge), whereas the minimum and the maximum values are represented by the top and bottom whiskers, respectively. The violin plot in Figure 1*C* represents the distribution of all the data points, with the midline representing the median value.

Results

M/TCs differentially respond to different frequencies in odor stimuli

We have previously shown that mice can behaviorally distinguish temporal structure in odors at frequencies up to 40 Hz (Ackels et al., 2021). Breathing in awake mice is highly variable versus almost metronomic in anesthetized animals. Thus, to precisely probe the effect of temporal structure in odor stimuli on M/TC activity, we recorded neural activity in anesthetized mice, linking odor stimulation to the rhythmic breathing. We recorded extracellular spiking activity using NeuroNexus silicone probes (97 units, 6 mice) from the dorsal OB while presenting four different odors (ethyl butyrate, 2-hexanone, amyl acetate, and eucalyptol) at five different frequencies (2, 5, 10, 15, and 20 Hz; Fig. 1*A*,*B*) using a high-speed odor delivery device we recently developed (Ackels et al., 2021). As M/TCs can respond to changes in air pressure because of mechanosensitivity of OSNs (Grosmaitre et al., 2007), we offset changes in flow by presenting an odorless air stream from an additional valve following a temporal

←

in spiking frequency in the first 500 ms after odor onset compared with the baseline for (from left to right) ethyl butyrate, 2-hexanone, eucalyptol presentation and isoamyl acetate presentation. The units have been sorted and grouped based on similarity in their activity for a given odor.

structure that operated anticorrelated to the odor valve. This resulted in approximately constant air flow profile throughout the odor presentation (Fig. 1*A*,*B*). The tODD allowed for a reliable odor pulse presentation (Fig. 1*B*) with similar net volumes of odor for all the frequencies ($p = 0.3142$, Welch's t test; Fig. 1*C*). To control for responses to residual flow changes, we included blank trials, that is, trials identical to the odor trials in temporal structure, except that both the valves were connected to vials filled with mineral oil. Respiration was continuously monitored using a flow sensor placed in close proximity to the nostril contralateral to the recording hemisphere. Respiration frequency was 2.8 ± 0.5 Hz (mean ± SD, $n = 6$ animals; Fig. 1*E*). To minimize sniff-cycle related variability (Shusterman et al., 2011), we triggered odor stimulation at the onset of inhalation. Further, we estimated the amount of odor that the animals might be inhaling during all the different frequencies. To do that we convolved the inhalation phase of every sniff cycle during the odor presentation with the recorded PID trace (Fig. 1*F*). We then compared the convolved value for every sniff for the entire duration of a given odor presentation for all the different odor frequencies (Fig. 1*G*, *I*). Next, we performed a pairwise statistical analysis among all the frequency combinations for a given sniff (Fig. 1*H*,*J*). We observe that the odor integral during the first sniff varies marginally albeit significantly between the slow frequencies (2 and 5 Hz) and the fast frequencies (10–20 Hz; Fig. 1*H*), whereas from the second sniff onwards there is no significant difference (Fig. 1*J*). Further, we did not find any statistical significance between the slow 2 and 5 Hz or among the fast 10, 15, and 20 Hz frequencies.

A typical recording session yielded recordings from multiple clusters from a depth of 300–500 μm from the OB surface. The recorded clusters were classified either as good (well isolated clusters), MUA (clusters that contained spikes of physiological origin but from numerous cells), or noise (clusters containing spikes of nonphysiological origin, e.g., electrical interference, movement artifacts) based on their autocorrelograms (Fig. 2*D*,*E*, left), waveforms (Fig. 2*D*,*E*, middle), firing rate and amplitude stabilities. Depending on the odor identity, between 49 and 72% of units displayed significant changes ($p < 0.05$, Mann–Whitney U test) in their firing rates in response to the stimuli (ethyl butyrate, 70/97; 2-hexanone, 72/97; amyl acetate, 56/97; eucalyptol, 48/97; Fig. 2*B*,*C*). Corroborating previous findings (Fukunaga et al., 2012; Jordan et al., 2018a,b; Ackels et al., 2020) we observed that most of the units also coupled distinctly to either the inhalation (Fig. 2*D*, right, *F*) or exhalation phase (Fig. 2*E*, right, *F*) of the sniff cycle. From the entire population of recorded units, we estimated a total of 64 pTCs and 26 pMCs, whereas seven units could not be resolved into either of the class (Fig. 2*F*). The average baseline firing of the recorded units was found to be 11 ± 9 Hz (mean ± SD; Fig. 2*K*).

Importantly, a subset of units displayed visibly different spiking profiles in response to different frequency odor stimuli (Fig. 2*G*,*H*). Comparing activities of units between 2 and 20 Hz stimuli, we observed that a substantial number of units showed significant difference in their activity in the first 500 ms after odor onset when compared with their response to the blank stimuli. This was true for all the four odors tested (ethyl butyrate, 22/97; 2-hexanone, 13/97; amyl acetate, 28/97; eucalyptol, 15/97; blank, 9/97; $p < 0.01$ Mann–Whitney U test; Fig. 2*I*). However, we did not find any obvious pattern between units responding for a given frequency among all the odors (Fig. 2*L*).

To examine the population-level response to these different stimuli, we constructed response vectors by computing the cumulative spike count for all the 97 recorded units in the first 500 ms after odor onset and subtracting from it the spike counts of a blank trial. We trained linear classifiers on 80% of the data and tested on 20% to examine whether spiking activity obtained for different stimulus frequencies was linearly separable (Fig. 3*A*). We observed that when we used a 500 ms rolling window with temporal steps of 10 ms, a classifier could achieve peak accuracies (ethyl butyrate, 0.55 ± 0.08; 2-hexanone, 0.51 ± 0.08; amyl acetate, 0.53 ± 0.08; eucalyptol, 0.45 ± 0.08) notably higher than what was obtained by training on shuffled data (0.2 ± 0.07; Fig. 3*B*). In addition, we trained classifiers on random subsets of unit responses, binned in a 500 ms window from odor onset. The classifier accuracies increased with an increasing number of units, with peak accuracies found for classifiers that had the full set of units available (ethyl butyrate, 0.41 ± 0.05; 2-hexanone, 0.35 ± 0.05; amyl acetate, 0.46 ± 0.05; eucalyptol, 0.39 ± 0.05) compared with shuffled data (0.2 ± 0.05; Fig. 3*C*). We then trained a series of classifiers to distinguish pairs selected from all possible combinations of odor frequencies and identities. We found that classifiers could readily distinguish responses for different stimulus frequencies well above chance (>0.5) for a given odor and performing even better when comparing responses for trials across different odors (Fig. 3*D*). Next, we withheld one trial of each type of stimuli and trained a classifier with all the remaining trials. We tested the classifier on the withheld trials to see both how well it could distinguish trials, as well as explore the structure of the false classifications (Fig. 3*E*). For a given odor, the predictability of a frequency of stimulus reached well above chance (>0.04). Furthermore, when comparing across the different odors, the predictability was almost perfect (Fig. 3*E*). Next, we trained classifiers based on the response of every unit to all the four odors for the five different frequencies. Each of the classifiers had access to the response of a single unit for a single odor. The average accuracy obtained from all the odors for a given unit were sorted and plotted (Fig. 3*F*). We could observe that both the pTCs and pMCs appeared at different accuracy values indicating that both the cell population responses were required to achieve the overall final accuracy values for the population. One should note, however, that the number of pTCs recorded were much larger than the number of pMCs.

Overall, this suggests that OB neurons can encode temporal structure present in odor stimuli at frequencies of at least up to 20 Hz in their spiking pattern. Importantly, this indicates that information can be read out by downstream structures simply by summing activity over populations of M/TCs at relatively low temporal resolution (i.e., spike counts over 500 ms).

M/TCs follow odor stimulus both at 2 and 20 Hz

To better understand the mechanism that gives rise to frequency-dependent M/TC spiking responses and to get insight into their subthreshold basis, we performed whole-cell recordings from M/TCs (Fig. 4*A*). To increase the probability of finding a responsive cell-odor pair and because of the time limitation and lower yield of stable whole-cell recordings, we used odor mixtures as stimuli (A, ethyl butyrate and 2-hexanone; B, amyl acetate and eucalyptol) and presented odors at only two frequencies, 2 and 20 Hz (Fig. 4*E*). As with the unit recordings, stimuli were triggered at the onset of inhalation, and blank trials were included. The animals had an average respiration frequency of 2.9 ± 1.3 Hz (mean ± SD, $n = 25$ mice; Fig. 1*D*). We recorded from 42 neurons in 25 mice at depths of 180–450 μm from the surface of the olfactory bulb (Fig. 4*B*). The neurons showed resting membrane potentials (RMP) ranging from −38 mV to −60 mV (Fig. 4*C*) and input resistance of 45–280 MΩ (Fig. 4*D*).

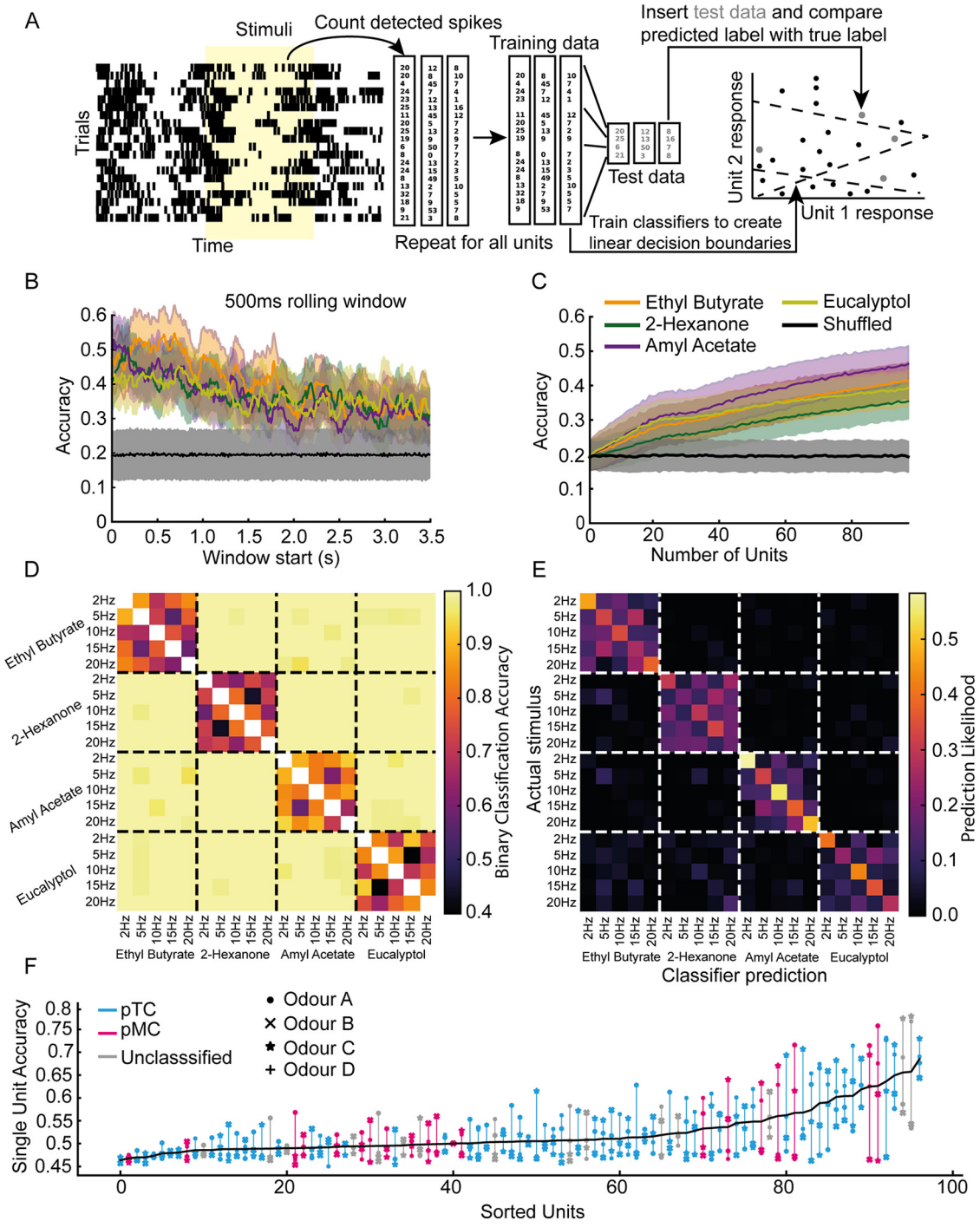

Figure 3. Classifiers to unit responses. ***A***, Schematic outlining of the procedure to train classifiers on unit spike times following an odor stimulus. ***B***, Average accuracy of linear SVM classifiers trained on a summed 500 ms rolling window of detected unit spikes from different start times after odor onset. ***C***, Average accuracy of a set of linear SVM classifiers trained on the summed response from units 500 ms from odor onset as the number of units available increases. ***D***, Matrix of all possible one versus one comparisons between different trial types and the average accuracy of a linear SVM trained to distinguish between the two. Chance is 0.5. ***E***, A confusion matrix of linear fractional classifications for a set of classifiers trained to distinguish all trial types from one another. The *y*-axis represents the true label of a trial, and the *x*-axis represents the given label of a classifier to a trial. Chance is 0.04. ***F***, The single-cell responses to all four odors were used to train classifiers to distinguish responses to 2 and 20 Hz. Each classifier only had access to the responses of a single unit to a single odor. The accuracies from these classifiers were averaged across the four odors and used to sort the units. Each vertical line connects the accuracies to classifiers trained on the same unit but to different odors. Each odor is represented by a different symbol. The vertical lines and symbols are colored by the putative cell classification of each unit, cyan (pTCs), magenta (pMCs), or unknown (gray).

These values are congruent with previous findings indicating that our recordings were largely from M/TCs (Margrie et al., 2001, 2002; Margrie and Schaefer, 2003; Fukunaga et al., 2012; Jordan et al., 2018a,b). In response to 2 Hz odor presentation, 25/70 cell-odor pairs showed significant changes in action potential discharge compared with the blank stimulus at the same frequency in the first 500 ms after odor onset (13/35 for Mixture A, 12/35 for Mixture B). Of these, 14/25 cell-odor pairs significantly increased their firing in response to odor stimulation, whereas 11/25 showed a significant decrease. To assess the subthreshold response, we calculated the average change in membrane potential (Δ Voltage) during the first

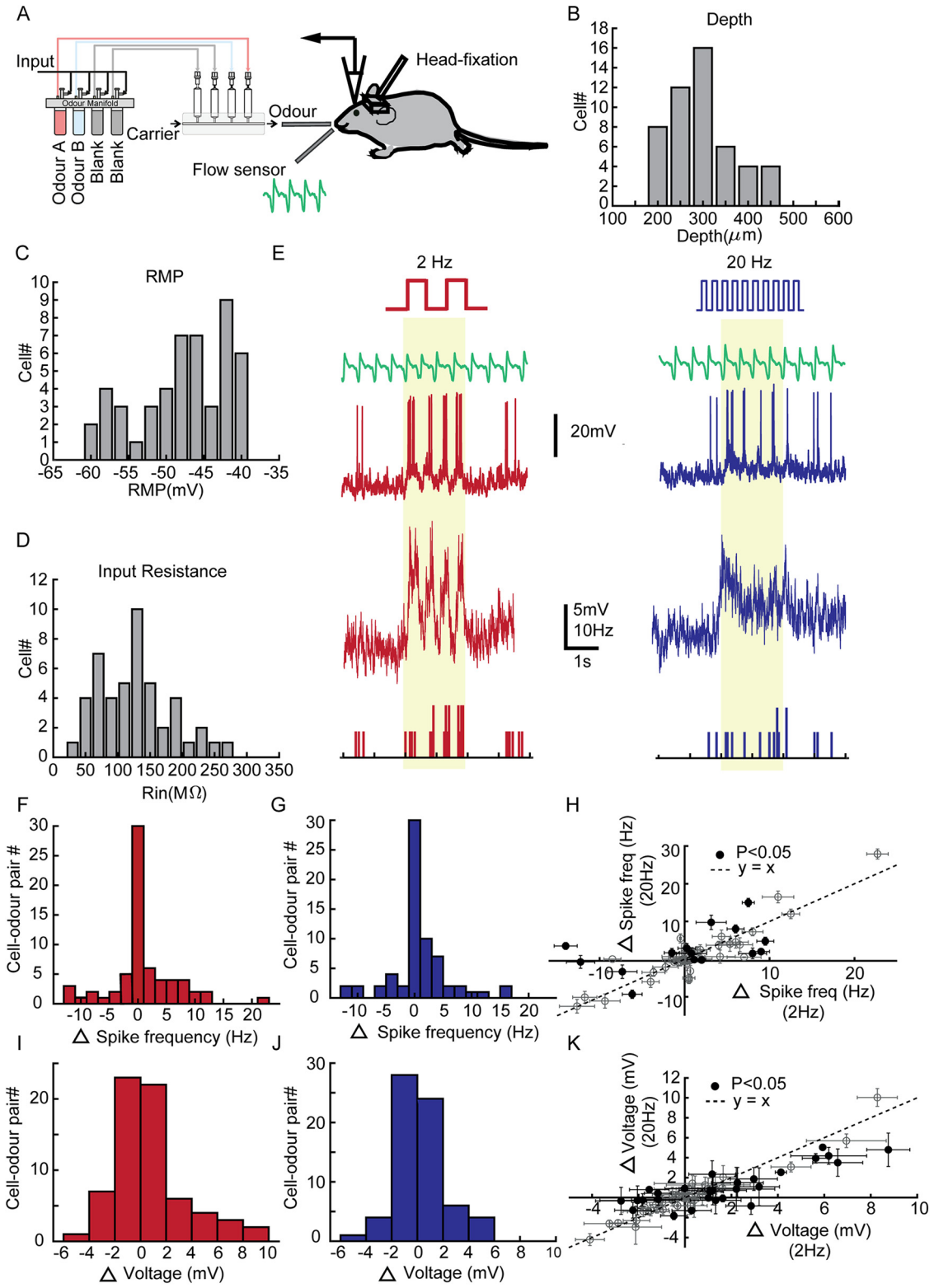

Figure 4. OB neurons respond to both 2 and 20 Hz temporally structured odor stimuli. ***A***, Schema of the whole-cell recording experimental setup. ***B***, Histogram representing the distribution of depth from the OB surface of all the recorded neurons. ***C***, ***D***, resting membrane potential (***C***) and input resistance (***D***; $n = 42$ cells, 25 mice). ***E***, Example recordings for 2 Hz (left) and 20 Hz (right) stimuli. Top to bottom, Schema of odor stimulus, example respiration trace, example recording from a neuron, extracted V_m and PSTH. ***F***, ***G***, Histogram of change in action potential frequency in the first 500 ms compared with the baseline for 2 Hz stimuli (***F***) and 20 Hz stimuli (***G***). ***H***, Spike frequency change for 2 Hz versus 20 Hz for all cell-odor pairs. The hollow circles represent cell-odor pairs that showed a statistically insignificant difference between the 2 Hz and the 20 Hz trials, whereas the solid markers (15/70) represent cell-odor pairs showing a significant difference ($p < 0.05$, 2-tailed unpaired *t* test). Each marker represents a cell-odor pair, and the error bars represent the SD obtained from all the trials. ***I***, ***J***, Histogram of change in average V_m in the first 500 ms compared with the baseline for 2 Hz stimuli (***I***) and 20 Hz stimuli (***J***). ***K***, Average change in V_m for 2 Hz versus 20 Hz. The markers and error bars have similar meaning as in ***H*** but for change in V_m from baseline. Twenty-seven of 70 cell odor pairs showed a significant difference between the 2 and 20 Hz trials ($p < 0.05$, 2-tailed unpaired *t* test).

500 ms of the stimulus from the baseline. With 2 Hz odor presentation, 34/70 cell-odor pairs showed significant subthreshold responses compared with the blank stimulus at 2 Hz (24/34 for Mixture A, 10/34 for Mixture B). Of these, 18/34 cell-odor pairs significantly depolarized, and 16/34 hyperpolarized in response to odor stimulation. When presented with the 20 Hz odor stimulation, 18/70 cell-odor pairs showed significant spiking responses compared with the blank stimulus at 20 Hz (12/18 for Mixture A, 6/18 for Mixture B). Of these, 11/18 cell-odor pairs significantly increased their firing in response to odor stimulation, whereas 7/18 showed a significant decrease. On the subthreshold level, 25/70 cell-odor pairs showed significant odor responses to the 20 Hz odor stimulation (18/25 for Mixture A, 7/25 for Mixture B). Of these, 15/25 cell-odor pairs significantly depolarized in response to the odor stimulation, and 10/25 hyperpolarized.

Comparing the average change in action potential firing frequency in the first 500 ms after odor onset from the baseline between the 2 and 20 Hz responses (Fig. 4*F–H*) we observed that for 15/70 cell-odor pairs, responses differed significantly between the two cases (Fig. 4*H*; $p < 0.05$, two-tailed unpaired *t* test). For 6/15 cell-odor pairs, responses were significantly larger for the 2 Hz case. This is consistent with our findings from the unit recordings (Figs. 2, 3). Interestingly, a larger number of cell-odor pairs (27/70) showed significant differences between the subthreshold responses to the two stimuli (Fig. 4*I*,*K*; $p < 0.05$; two-tailed unpaired *t* test) compared with the suprathreshold response (18/27 cell-odor pairs showed significantly larger Δ Voltage responses for the 2 Hz stimulus).

To quantify the coupling of membrane potential to the frequency of odor stimulation, we estimated the peak correlation coefficient of the odor period (CC_{odor}) and compared with that for the blank condition (CC_{blank}; Fig. 5*H*,*I*). We observed that 20/70 (Fig. 5*H*) and 16/70 (Fig. 5*I*; 2 and 20 Hz respectively) showed a significant difference between CC_{odor} and CC_{blank}. Further, only 1/20 cell-odor pair among the ones showing significant change in the 2 Hz case showed a CC_{blank} higher than the CC_{odor}. This might be because of the residual respiration coupling left for this particular case.

To avoid the issue of the residual-respiration-driven membrane potential coupling contaminating the stimulus-driven coupling, we computed a C*p*C (Fig. 5*A–F*) for each individual cell ($n = 42$ cells, 70 cell-odor pairs, 25 mice; see above, Materials and Methods). In brief, to calculate C*p*C, the membrane potential was first baseline subtracted to minimize sniff-related membrane potential oscillations (Abraham et al., 2010; Fig. 5*G*). For a given cell-odor pair, C*p*C was then obtained by normalizing the peak cross-correlation value for the odor response to that for the mineral oil response (Fig. 5*C–F*), resulting in a C*p*C value >0. A high C*p*C value indicates a cell that has a strong cell-odor frequency coupling relative to the baseline. Further, a C*p*C >1 suggests that response of a cell to the odor-frequency pair is stronger than that to a blank trial and is not because of a response of a potential residual purely mechanical stimulus. A subset of the recorded cell-odor pairs showed C*p*C >1 suggesting possible coupling to both 2 Hz (35/70; Fig. 5*J*) and 20 Hz (25/70; Fig. 5*N*). To assess statistical significance of this coupling measure, we estimated the C*p*C of all the baseline periods for a given cell and compared with the ones obtained for the odor period for all the trials (Fig. 5*K*,*O*). Comparing the C*p*C between the original and the baseline, we observed that a substantial number of M/TC-odor pairs indeed significantly coupled to both 2 Hz (29/70 cell-odor pairs; Fig. 5*L*) and 20 Hz (24/70 cell-odor pairs; Fig. 5*P*; $p < 0.05$, two-tailed unpaired *t* test; all these were cell-odor pairs where we had observed significant subthreshold odor-evoked responses as defined above). However, we observed that 2/29 and 1/24 (2 and 20 Hz, respectively) cell-odor pairs among the significantly coupled ones showed a decrease in C*p*C for the odor stimulus compared with the baseline condition. For a subset of recorded cells, we presented a third stimulus, a continuous odor (with no temporal structure) and estimated the C*p*C as before. As expected, C*p*Cs obtained from the 2 and 20 Hz stimuli was significantly higher than that from the constant odor stimulus for a substantial portion of the recorded M/TCs (2 Hz, 17/32 cell-odor pairs; 20 Hz, 13/26 cell-odor pairs; $p < 0.01$, two-tailed paired *t* test, Fig. 5*M*,*Q*).

Depth of recording correlated with C*p*C

We next asked whether the C*p*C was related to the intrinsic properties of the recorded cells. We observed that input resistance (Fig. 6*A*,*B*) and RMP (Fig. 6*C*,*D*) of a cell were not correlated with its C*p*C. C*p*C and depth showed different correlations for 2 and 20 Hz. For the 2 Hz cases, we could not find any correlation between depth and C*p*C (Fig. 6*E*), whereas C*p*C decreased with depth for the 20 Hz cases (Fig. 6*F*; $p = 0.03$, odor A; $p = 0.019$, odor B; two-tailed test). This suggests that tufted cells, which are located more superficially than mitral cells, might couple more strongly to high-frequency (20 Hz) odor stimuli. Overall, however, C*p*C was only weakly dependent on intrinsic cellular properties.

Putative tufted cells show higher C*p*C than putative mitral cells

Spontaneous oscillation of membrane potential has been observed to be a reliable predictor of projection neuron type in the OB (Fukunaga et al., 2012; Jordan et al., 2018b; Ackels et al., 2020). We classified the recorded neurons into 23 pMCs and 17 pTCs based on the phase locking of the spontaneous membrane potential to the respiration cycle of the mouse (Fig. 7*A*,*B*). Two of the cells could not be resolved. Although overall similar, pTCs tended to couple marginally more strongly to the odor stimuli than pMCs, reaching significance for the 20 Hz case (2 Hz, $CpC_{pTC} = 1.32 \pm 0.48$, mean ± SD), $CpC_{pMC} = 1.24 \pm 0.41$; $p = 0.6476$, Kolmogorov–Smirnov test; 20 Hz, $CpC_{pTC} = 1.12 \pm 0.29$, $CpC_{pMC} = 0.95 \pm 0.49$; $p = 0.0436$, Kolmogorov–Smirnov test). This was consistent with the depth-based classification, where we observed that for the 20 Hz cases, superficially located (putative tufted) cells showed higher C*p*C compared with the deeper cells (putative mitral cells; Fig. 6*F*). However, we did not observe any significant difference in the lag of the peak correlation point between pTC and pMC ($p = 0.6297$, 2 Hz; $p = 0.6634$, 20 Hz, unpaired *t* test; Fig. 7*G*,*H*).

C*p*C for odor mixtures can be linearly predicted from that of individual constituents

As described above, we presented two different odor stimuli at different frequencies (odor A and odor B). Comparing C*p*Cs for odor A with that displayed for odor B, we noticed that these were tightly linked; M/TCs coupling well to odor A also coupled well to odor B, whereas M/TCs poorly coupling to one also coupled weakly to the other (Fig. 8*A*,*B*). This was the case for both 2 Hz (Fig. 8*C*) and 20 Hz (Fig. 8*D*) suggesting that the frequency coupling of a cell is independent of the odor presented. To further corroborate that C*p*C is an odor-independent parameter, we probed M/TCs with a mixture of the two odors. If frequency coupling is indeed odor independent, response of a cell

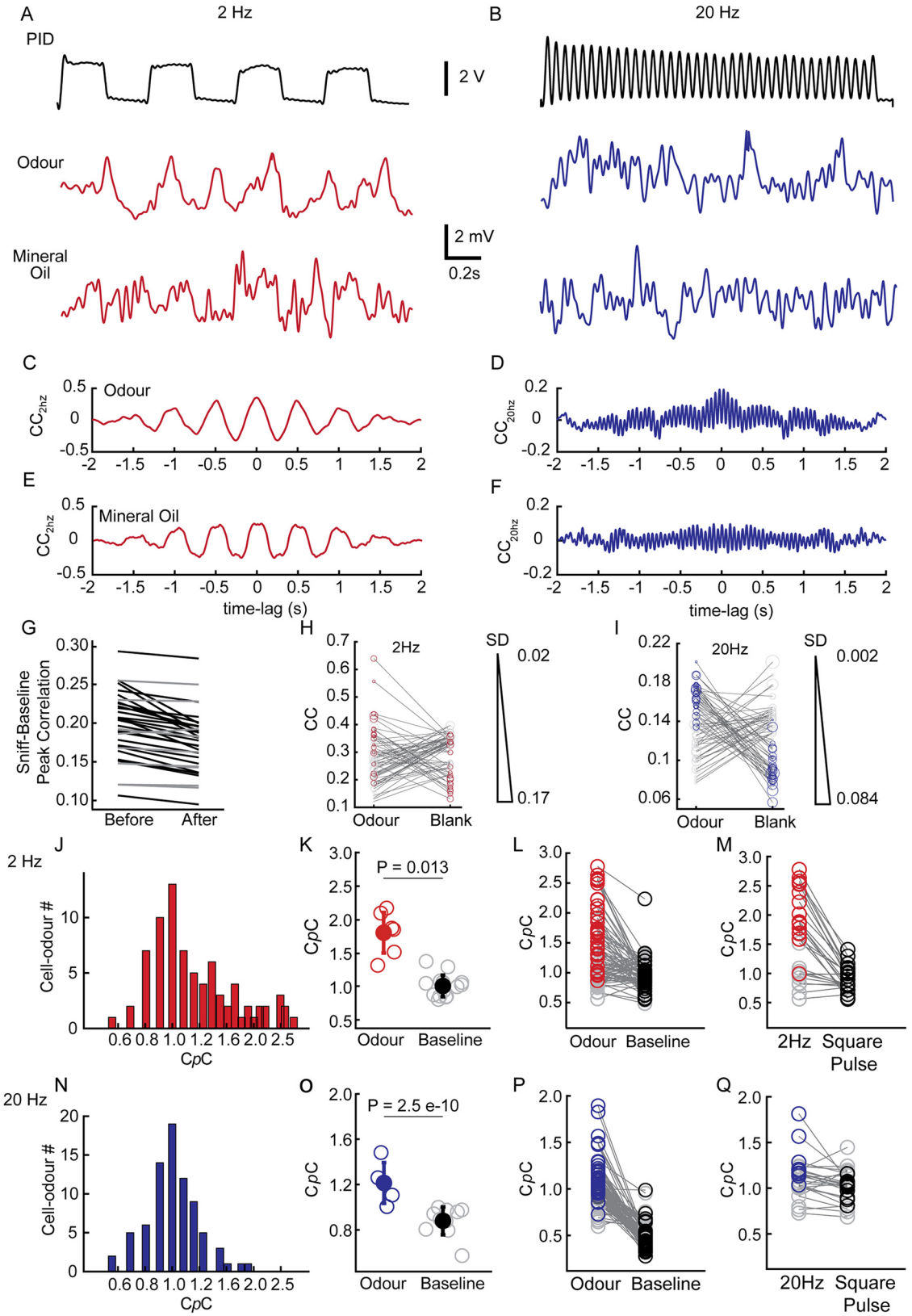

Figure 5. Olfactory bulb neurons can follow temporally structured odor stimuli. ***A***, Top, Example trace recorded using a PID of a 2 Hz odor stimulus. Middle, Example V_m trace (action potentials clipped and baseline subtracted) recorded during 2 Hz odor stimulus presentation, Bottom, Recording from the same neuron during 2 Hz mineral oil stimulus presentation. ***B***, Same as in ***A*** but for a 20 Hz stimulus from a different neuron. ***C***, Cross-correlation plot between 2 Hz PID trace and 2 Hz V_m odor trace. ***D***, Twenty-hertz PID trace and 20 Hz V_m odor trace. ***E***, ***F***, Two-hertz PID trace and 2 Hz V_m mineral oil trace (***E***) and 20 Hz PID trace and 20 Hz V_m mineral oil trace (***F***). ***G***, Mean peak correlation coefficient of the baseline period with the respective respiration stretches (2 s) plotted as before and after the subtraction operation. Black lines denote cells showing significant decrease in correlation after the correction (34/42, $p < 0.05$, paired t test). ***H***, CC_{odor} and CC_{blank} in cell-odor pair basis for the 2 Hz case. Red open circles mark the cell-odor pairs that showed significant difference compared with the blank trials ($n = 20/70$; $p < 0.05$, 2-tailed t test). ***I***, Same as in ***H*** but for the 20 Hz case. Blue open circles mark the cell-odor pairs that showed significant difference compared with the blank trials ($n = 16/70$; $p < 0.05$, 2-tailed t test). The marker size denotes the SD obtained from all the trials for a given

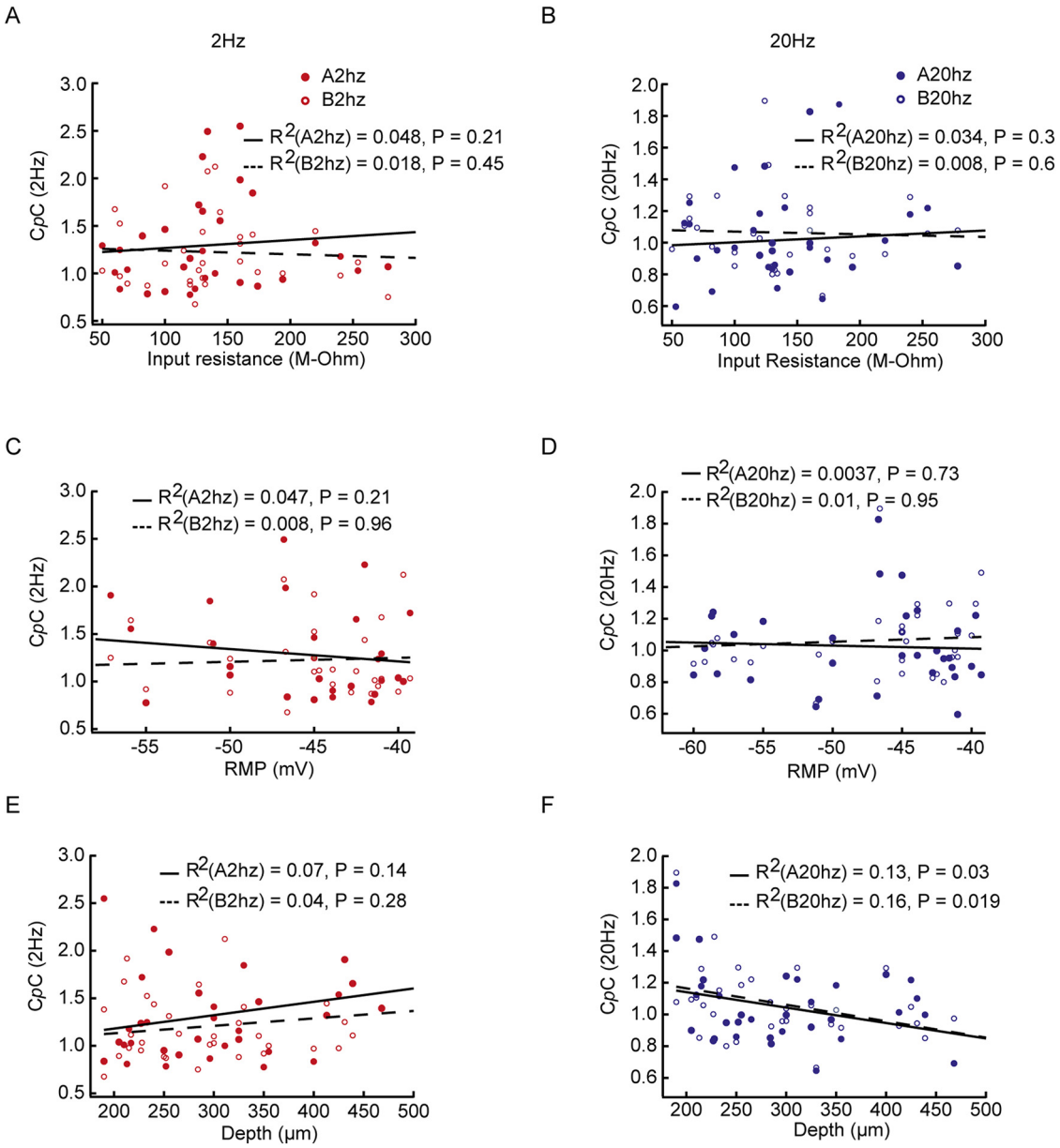

Figure 6. Cellular intrinsic properties do not explain the C*p*C of a cell. ***A***, ***B***, C*p*C versus input resistance for the 2 Hz (***A***) and 20 Hz case (***B***). ***C***, ***D***, C*p*C versus RMP for the 2 Hz (***C***) and 20 Hz case (***D***). ***E***, ***F***, C*p*C versus recording depth from the OB surface for the 2 Hz (***E***) and 20 Hz case (***F***). Note that with increasing depth of recording, the estimated C*p*C significantly decreased for the 20 Hz cases, indicating TCs couple more to 20 Hz odor stimulation than MCs.

←

cell-odor pair. ***J***, Histogram of C*p*C for all cell-odor pairs for 2 Hz responses ($n = 70$ cell-odor pairs, 25 mice). ***K***, C*p*C estimated from the individual odor trials (red open circle) and that from the baseline control (gray) of 2 Hz odor stimuli for a given cell-odor pair. The filled circle represents the population average of C*p*C obtained from the odor trials (red solid) and the baseline controls (black; $p = 0.013$, unpaired *t* test). ***L***, Odor C*p*C versus baseline C*p*C from all recorded cell-odor pairs. The gray markers ($n = 41/70$) represent the cell-odor pairs showing nonsignificant difference between the two, whereas the colored markers (29/70) represent the significantly different cell-odor pairs. Significance threshold was set at $p < 0.05$. ***M***, Estimated C*p*C for a subset of cell-odor pairs that were provided with both the temporal stimulus and square pulse. Note the significant decrease in C*p*C for the square pulse compared with the 2 Hz case. The red-colored open circles denote cell-odor pairs for 2 Hz, which showed significant difference from their paired square pulse trials (black open circles; 16/27 cell-odor pairs; $p < 0.05$; 2-tailed paired *t* test). ***N***, Same as in ***J*** but for 20 Hz responses. ***O***, Same as in ***K*** but for 20 Hz responses ($n = 24/70$, significant cell-odor pairs). ***P***, Same as in ***L*** but for 20 Hz responses. ***Q***, Same as in ***M*** but for the 20 Hz case. The blue-colored open circles denote cell-odor pairs for 20 Hz, which showed significant difference from their paired square pulse trials (black open circles; 13/27 cell-odor pairs; $p < 0.05$; 2-tailed paired *t* test).

to odor mixtures should be predictable from the C*p*C for the individual odor. To assess this, we first categorized recordings based on the direction of average change in membrane potential in the first 500 ms after odor onset and classified responses into the following three types: excitatory-inhibitory (Ex-In), excitatory-excitatory (Ex-Ex), and inhibitory-inhibitory (In-In; Fig. 9*A*,*B*). Notably, we did not observe any significant difference between C*p*Cs for the different response types, neither for 2 Hz ($p = 0.54$, one-way ANOVA; Fig. 9*C*) nor for 20 Hz ($p = 0.15$, one-way ANOVA; Fig. 9*D*).

Next, we tried to predict the C*p*C of a given cell to an odor mixture, based on the C*p*C of the cell obtained from the constituent odors. As predicted from the observation that C*p*C is largely cell intrinsic and odor independent, we observed that the C*p*C for a given cell-mixture pair could be reliably predicted from the cell-constituent pairs both for 2 Hz ($p = 1.3 \times 10^{-9}$, two-tailed test; Fig. 9*E*) and 20 Hz ($p = 1.81 \times 10^{-6}$, two-tailed test; Fig.

9*F*). Notably, we observed that C*p*C was not correlated with the strength of odor response for a given cell-odor pair (data not shown).

Influence of inhibition on C*p*C

Because our observations indicated that C*p*C is cell intrinsic, independent of the odor presented (Figs. 8, 9) and was only weakly dependent on intrinsic cellular properties (Fig. 6), we next asked whether the C*p*C of a cell was shaped by circuit properties.

OB inhibitory circuits are known to shape M/TC activity and odor responses (Yokoi et al., 1995; Fukunaga et al., 2012, 2014; Burton, 2017). To assess the role that circuit-level inhibition may have on cellular C*p*C, we recorded from M/TCs as outlined previously and then washed in a titrated mixture of 0.4 mM gabazine and 2 mM muscimol to cause $GABA_A$ clamping (Fukunaga et al., 2012), blocking synaptic inhibition while providing sufficient unspecific background inhibition to avoid epileptic discharge. Following a short period of change in membrane potential, the recorded neurons returned to approximately their original RMP within a few minutes (Fig. 10*A*). The input resistance (Fig. 10*E*) and RMP (Fig. 10*H*) did not change significantly in any of the neurons recorded. Under baseline conditions before GABA clamping, the estimated C*p*C was significant compared with the baseline control for most of the recorded cell-odor pairs (13/15; 2 Hz and 14/15; 20 Hz, $p < 0.01$, two-tailed paired *t* test). Postdrug perfusion (with $GABA_A$ clamp) all recorded cells were significantly coupled (15/15; 2 and 20 Hz, $p < 0.01$, two-tailed paired *t* test; Fig. 10*C*,*D*). Furthermore, we noticed a significant change in C*p*C for most of the cell-odor pairs postdrug treatment from their baseline values ($n = 10/15$; 2 Hz and 9/15; 20 Hz, $p < 0.01$, two-tailed paired *t* test; Fig. 10*F*,*G*). Interestingly, this shift in C*p*C post-$GABA_A$ clamping happened in both directions with 5/15 cell-odor pairs showing a significant decrease and 5/15 a significant increase in their C*p*C values in the 2 Hz case (Fig. 10*F*). For the 20 Hz case, we observed that 2/15 cell-odor pairs showed a decrease, whereas for 7/15, C*p*C values increased (Fig. 10*G*). Furthermore, we observed that cell-odor pairs that showed a significant increase in C*p*C post-$GABA_A$ clamp from their baseline values largely had initial C*p*C <1 (2 Hz, 0.947 ± 0.076; 20 Hz, 0.98 ± 0.11, mean ± SD), whereas for cell-odor pairs showing a decrease post-$GABA_A$ clamp had initial C*p*C >1 (2 Hz, 2.31 ± 0.39; 20 Hz, 1.3 ± 0.07, mean ± SD). Overall, our results indicate that the local inhibitory circuitry contributes significantly to determining the C*p*C of a cell.

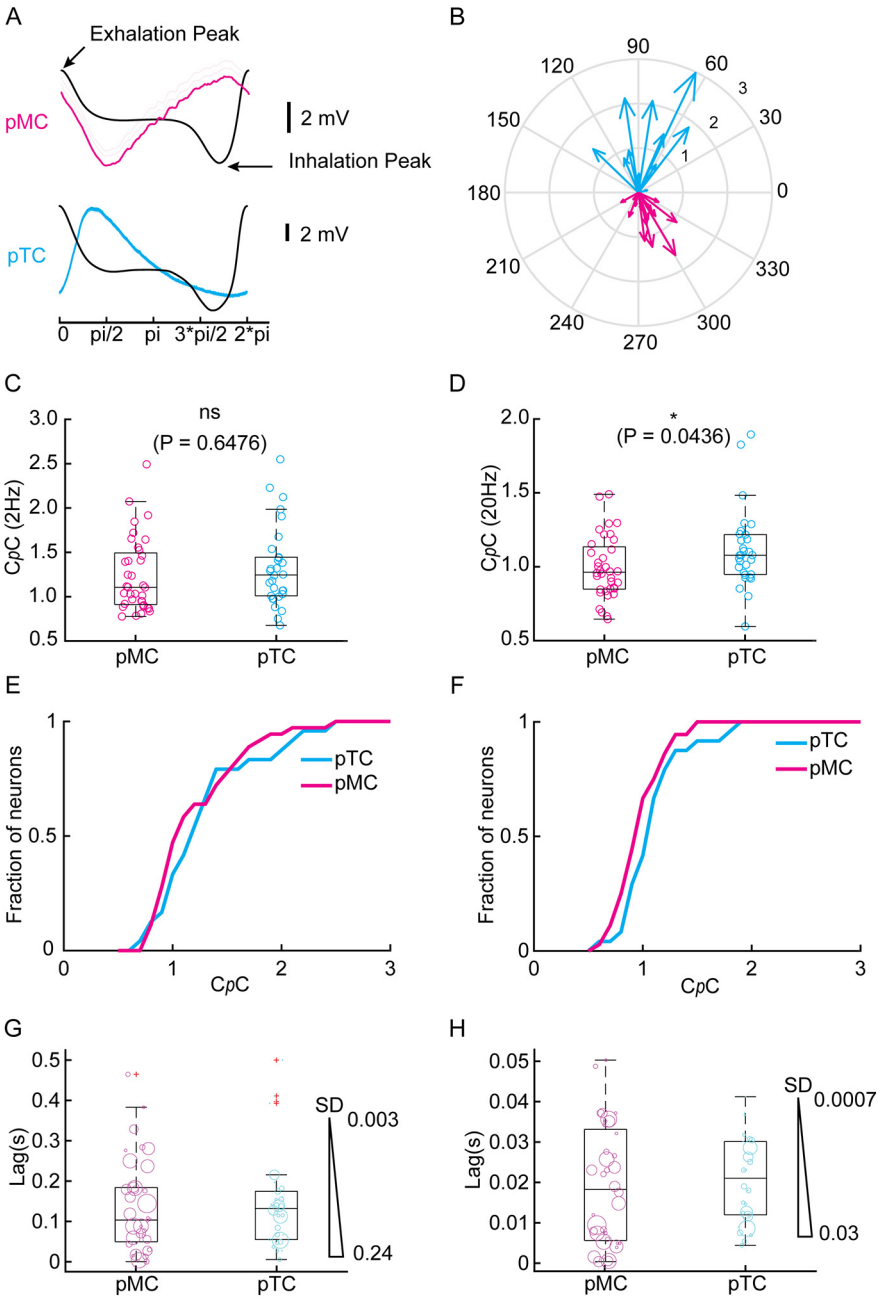

Figure 7. The putative tufted cells show higher probability of following 20 Hz stimulus but not 2 Hz stimulus compared with putative mitral cells. ***A***, Top, Example baseline average V_m trace from a putative mitral cell (magenta) overlaid with average sniff cycle (black). Bottom, Similar traces for a putative tufted cell (cyan). ***B***, Summary phase diagram of peak subthreshold oscillation phase plot (pTC, $n = 17$; pMC, $n = 23$). ***C***, C*p*C for all the recoded pTCs and pMCs for 2 Hz showing no significant difference between the two population ($p = 0.64$, Kolmogorov–Smirnov test). ***D***, pTCs show higher C*p*C than pMCs for 20 Hz cases ($p = 0.04$, Kolmogorov–Smirnov test). ***E***, ***F***, Cumulative histogram of C*p*C for all pTCs and pMCs for 2 Hz (***E***) and 20 Hz cases (***F***). ***G***, Lag of the peak correlation point for the 2 Hz case. The cyan and the magenta open circles represent individual pTC odor-pairs and pMC odor-pairs, respectively. The population did not show any significant difference ($p = 0.6297$, unpaired *t* test). The marker size denotes the SD obtained from all the trials for a given cell. ***H***, Same as in ***G*** but for the 20 Hz case ($p = 0.6634$, unpaired *t* test).

Discussion

Mammalian olfaction research has largely used odor identity (chemical structure) and intensity as modulators of odor responses despite the presence of rich temporal structure in

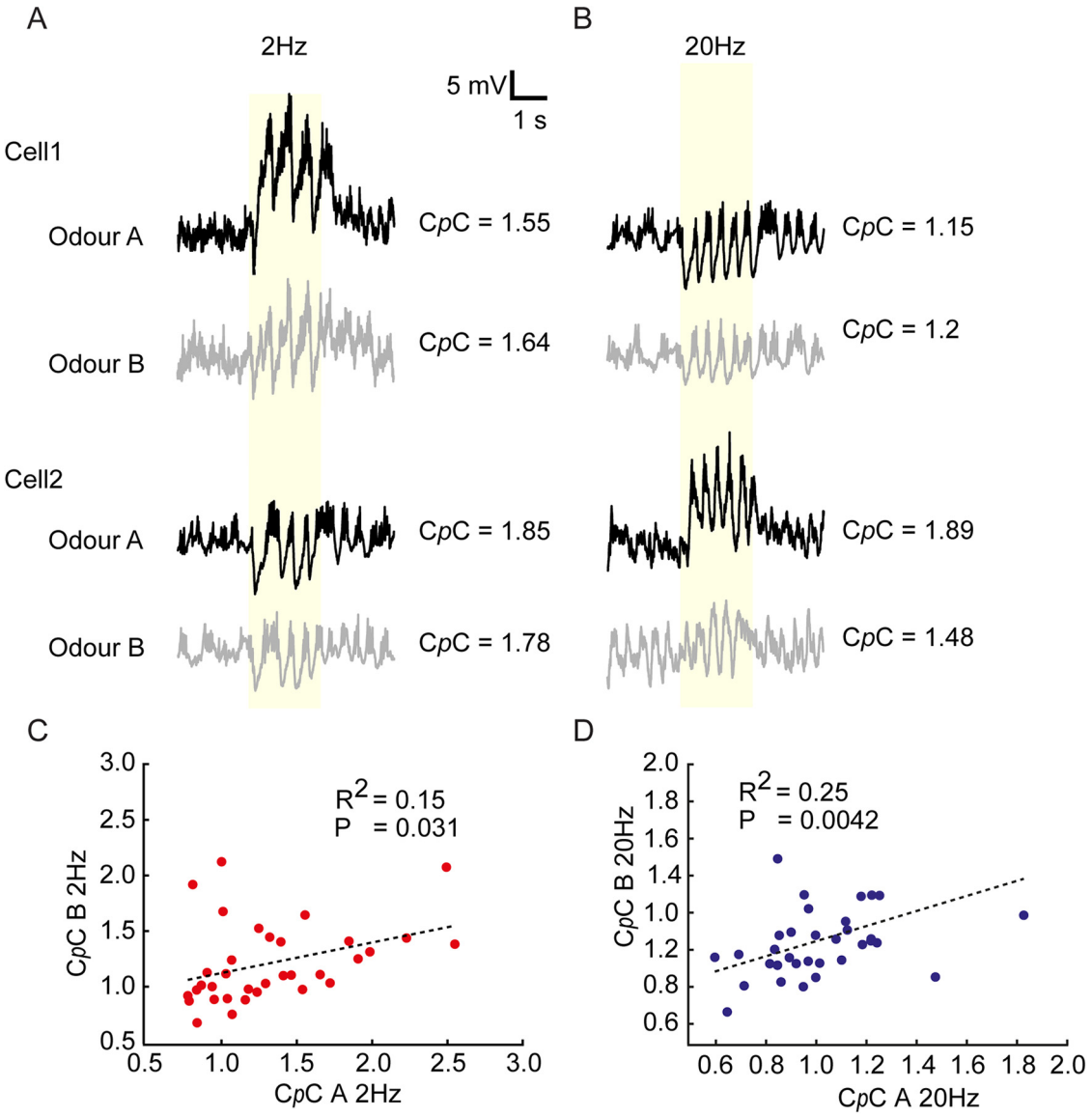

Figure 8. C*p*C is odor invariant. ***A***, Example recordings from two cells responding to both odors A and B at 2 Hz. Note that C*p*C values are similar for the two odors. ***B***, As in ***A*** for 20 Hz stimulation. ***C***, ***D***, Plot of estimated C*p*C A versus C*p*C B from all the recorded cells for 2 Hz (***C***) and 20 Hz (***D***) case. Note the strong correlation in both cases suggesting that coupling to frequency-modulated odor stimuli is odor independent.

natural odor landscapes. Here, we have shown that M/TCs in the OB *in vivo* can encode frequencies in odor stimuli as high as 20 Hz. Furthermore, whole-cell recordings indicated that a subset of M/TCs significantly couple to frequencies of odor stimuli both at the sniff range and subsniff range in a largely odor-independent manner. Importantly, although heterogeneous between cells, the strength of coupling is largely independent of the odor applied. We have demonstrated that odor frequency coupling capacity is similar between pMC and pTC populations at 2 Hz, whereas at 20 Hz, pTCs couple somewhat more strongly than pMCs. Finally, although coupling capacity is variable between cells but largely independent of specific intrinsic properties, we observed that inhibitory circuits strongly modulate the frequency coupling capacity of a cell. Overall, we show that the OB has the capacity to encode high-frequency temporal patterns present in olfactory stimuli. M/TCs vary in their propensity to follow temporally structured stimuli, and this depends on the local circuitry.

In mammals, respiration ensures a low-frequency, periodic sampling of olfactory stimuli, which in turn is the main source of theta activity in the early olfactory areas (Macrides and Chorover, 1972; Margrie and Schaefer, 2003; Schaefer et al., 2006). This causes rhythmic activity in M/TCs, even when devoid of odor stimuli (Grosmaitre et al., 2007; Connelly et al., 2015; Díaz-Quesada et al., 2018). Furthermore, the concentration of natural odor stimuli fluctuates in time (Riffell et al., 2008; Martinez and Moraud, 2013; Celani et al., 2014; Pannunzi and Nowotny, 2019; Ackels et al., 2021), providing an extra layer of temporal information to the input signal of the OB. Altogether, this creates temporally complex input signals for OSNs that are thought to carry information about the odor source (Hopfield, 1991; Vergassola et al., 2007; Celani et al., 2014; Ackels et al., 2021). Although signal transduction at the olfactory receptor neuron level is relatively slow (Ghatpande and Reisert, 2011), simulations have shown that OSN convergence into the OB can help sustain high-frequency information (Ackels et al., 2021), similar to encoding in the auditory system (Carr, 1993). Furthermore, correlated and anticorrelated odor stimuli were shown to be faithfully

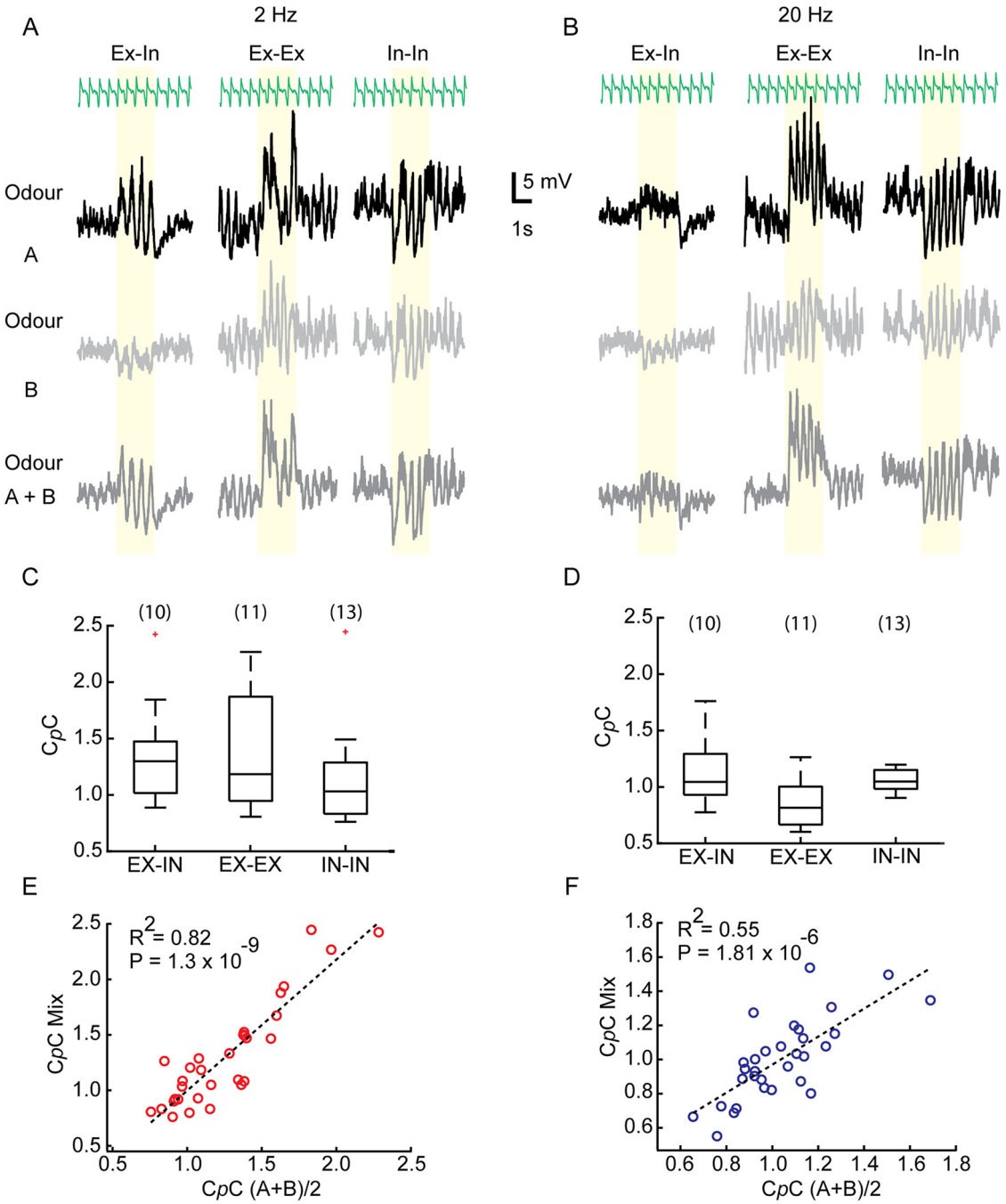

Figure 9. CpC for a mixture of odor can be linearly predicted from the individual component. ***A***, Example recordings for three different types of mixture interaction, Ex-In, Ex-Ex, and In-In. Top to bottom, Respiration trace, V_m for odor A, B, and A + B mixture delivered at 2 Hz. ***B***, As in ***A*** but for 20 Hz. ***C***, ***D***, No significant difference in CpC between the three types of mixture responses for 2 Hz (***C***) and 20 Hz (***D***). The numbers in brackets are the number of cells (1-way ANOVA, $p = 0.54$, 2 Hz; $p = 0.14$, 20 Hz). ***E***, ***F***, Computed CpC of odor (A + B)/2 versus actual CpC of mixture (A + B) for 2 Hz (***E***) cases and 20 Hz cases (***F***). Note linear regression can reliably predict the relation between calculated and estimated CpC ($n = 35$, $p = 1.3 \times 10^{-9}$, 2 Hz; $p = 1.81 \times 10^{-6}$, 20 Hz).

represented in the OB and resulted in distinct behavioral responses for frequencies up to 40 Hz (Ackels et al., 2021). Together with the aforementioned physiological (Cury and Uchida, 2010; Shusterman et al., 2011) and behavioral experiments using precise optogenetic stimuli (Smear et al., 2011; Li et al., 2014; Rebello et al., 2014), this suggests the presence of cellular and/or network mechanisms supporting the encoding of high-frequency natural odor stimuli. Previous reports have varied inhalation frequency via tracheotomy and shown that M/TCs followed the respiratory rhythm at frequencies up to 5 Hz (Díaz-Quesada et al., 2018; Short and Wachowiak, 2019; Eiting and Wachowiak, 2020). Here, we have shown that in naturally breathing mice M/TCs in the OB can follow odor fluctuations well exceeding respiration rate at frequencies of 20 Hz and that local circuit inhibition plays an important role in this encoding.

Functional implications

Naturally, odors are carried by turbulent plumes of wind or water generating filamentous fluctuations of odor concentration

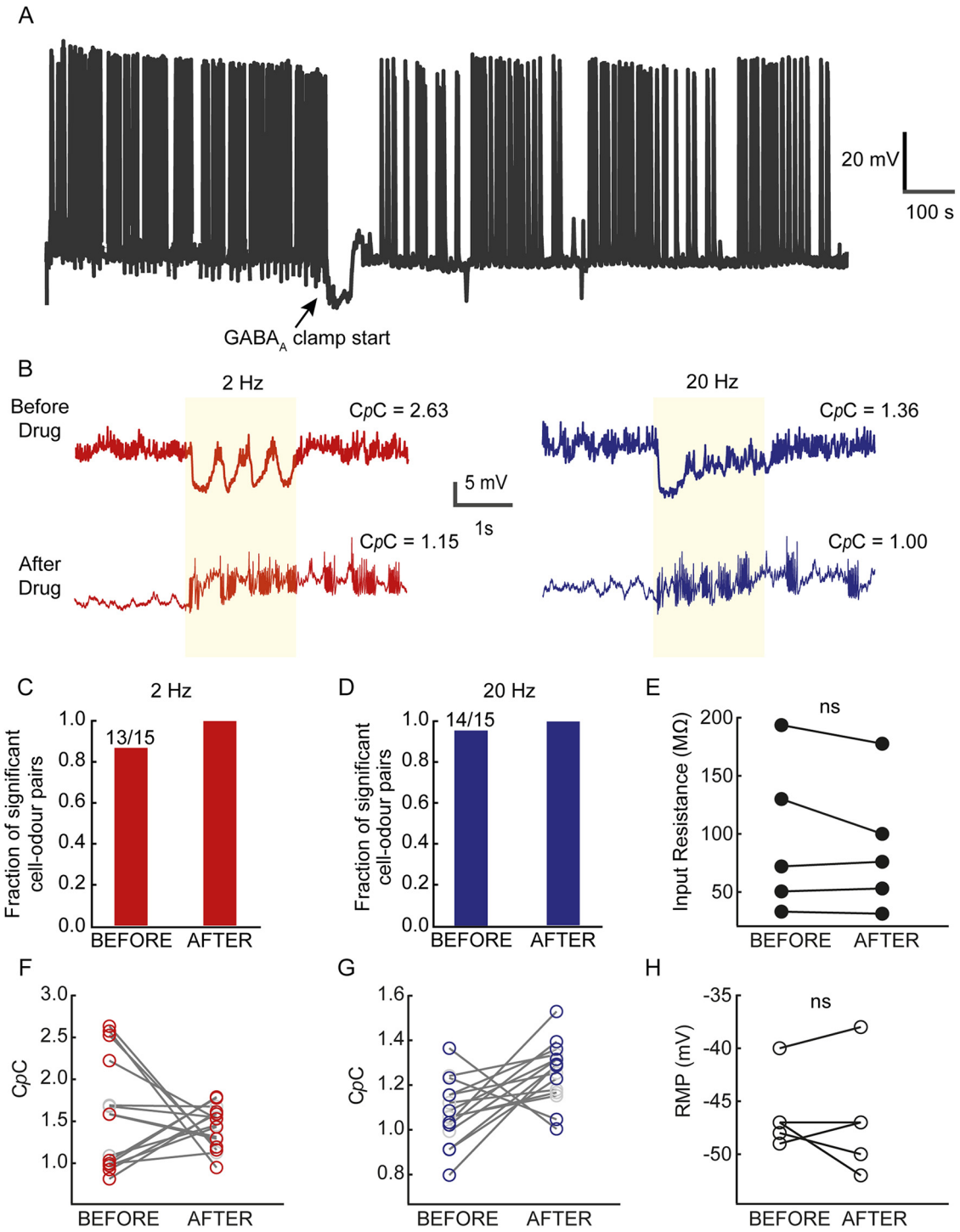

Figure 10. Influence of blocking inhibition on C*p*C. ***A***, Example recording showing time of 2 mM muscimol + 0.4 mM gabazine infusion for $GABA_A$ clamping. ***B***, Example V_m trace without drug (top) and after 10 min from drug infusion point (bottom) in a continuous recording for 2 Hz (red) and 20 Hz case (blue). ***C***, Fraction of cell-odor pairs showing significant C*p*C compared with their baseline control before and after the drug infusion point for 2 Hz stimuli. ***D***, Same as in ***C*** but for 20 Hz cases. ***E***, Input resistance of the recorded neurons estimated both before and after drug infusion ($n = 5$). No significant change was observed (paired *t* test, $p = 0.272$, (ns)). ***F***, Ten of 15 cell-odor pairs (red) showed significant change in their C*p*C post-$GABA_A$ clamping, whereas 5/15 (gray) showed no significant change in the 2 Hz case ($p < 0.01$, 2-tailed paired *t* test). ***G***, Nine of 15 cell-odor pairs (blue) showed significant change in their C*p*C post-$GABA_A$ clamping, whereas 6/15 (gray) showed no significant change in the 20 Hz case ($p < 0.01$, 2-tailed paired *t* test). ***H***, RMP of the recorded cells did not change significantly because of $GABA_A$ clamping (paired *t* test, $P = 0.313$, (ns)).

(Celani et al., 2014) that can in principle contain information about the nature and location of odor sources (Fackrell and Robins, 1982; Hopfield, 1991; Moore and Atema, 1991; Mylne and Mason, 1991; Vergassola et al., 2007; Schmuker et al., 2016; Ackels et al., 2021; Marin et al., 2021; Crimaldi et al., 2022). Our observations here indicate that the M/TCs reliably encode information about odor fluctuations at frequencies from 2 to 20 Hz (Figs. 2, 3, 5). Consistent with these results obtained from unit recordings, we observe that indeed a subset of neurons recorded intracellularly showed significantly different spiking

and subthreshold membrane potential activity when presented with 2 Hz or 20 Hz fluctuating odor stimuli (Fig. 5*K*,*O*). Furthermore, our read-out parameter, C*p*C, provides an estimate of how strongly a given neuron can directly couple to a specific odor frequency. Both types of projection neurons coupled equally to odors presented at 2 Hz (Fig. 7*C*), whereas tufted cells showed somewhat higher coupling than mitral cells to 20 Hz (Figs. 6*F*, 7*D*). It is possible that further physiological analysis with different temporally structured stimuli might reveal distinct subtypes of projection neurons. Recent reports have, for example, identified a subset of mitral/tufted cells specifically responsive to changes in concentration (Parabucki et al., 2019). Emerging molecular subtype division of projection neurons (Zeppilli et al., 2021) might reveal distinct groups of projection neurons following different temporal patterns of odor presentation. Considering the heterogeneity of projection targets, this might indicate that different postsynaptic regions receive differentially filtered information. Tufted cells, which in our hands showed stronger frequency coupling for 20 Hz, for example, preferentially project to anterior olfactory nucleus or anterior piriform cortex (Scott et al., 1980; Schneider and Scott, 1983; Nagayama et al., 2010). Further studies will be required to find exact structures in the downstream areas related to frequency-specific odor signal computation. The fact that blocking inhibition altered the frequency coupling capacity (Fig. 10) indicates that the inhibitory circuitry of the OB plays a strong role in shaping the encoding of temporal features. This is consistent with a previous finding in *Drosophila* projection neurons, where blocking presynaptic inhibition altered response kinetics for temporally dynamic odor stimuli (Nagel et al., 2015). Additionally, we observe that post-$GABA_A$ clamping, some of the cells displayed a decrease of C*p*C, whereas other cells showed an increase (Fig. 10*F*, *G*). Further studies are required to pinpoint the precise inhibitory pathway that might be responsible for modulating frequency coupling in M/TCs in a cell-to-cell basis and possibly identify subpopulations of MCs and TCs that encode specific temporal features.

Limitations of the study

All the recordings presented here were performed in anesthetized mice benefitting from the stability of respiration in this state. Previous reports suggested that the behavioral state affects mitral cell firing properties (Rinberg et al., 2006; Kato et al., 2012). However, studies have suggested that M/TC firing rates in awake conditions do not change but rather get redistributed over a breathing cycle (Gschwend et al., 2012). Whole-cell recordings from M/TCs indicate that membrane properties are largely similar between the two states (Kollo et al., 2014), consistent with recent unit recording results (Bolding et al., 2020). It will nevertheless be important to repeat these experiments in awake mice to probe whether the M/TCs hold to the same frequency coupling behavior as that found in anesthetized mice. Second, because of the time limitation of reliable whole-cell recordings, we could probe only two frequencies. Extracellular unit recording data partially alleviated this limitation by investigating additional intermediate frequencies. Linear classifiers performed at accuracies well above chance level (Fig. 3), suggesting that M/TCs can encode several frequencies up to 20 Hz. Therefore, it is likely that the frequency coupling capacity of subthreshold activity could span this range as well.

Temporally structured stimuli and pathophysiology

In addition to better replicating naturalistic stimuli, temporally patterned sensory stimuli have been found to be advantageous in treating diseases. Although direct electrical (and more recently optical) rhythmic deep brain stimulation is recognized as a possible treatment for a variety of neurodegenerative diseases (Benabid et al., 1987; Laxton et al., 2010; Zhang et al., 2019), it is only quite recent that temporally modulated sensory stimulation has been used in a similar manner. For example, using 40 Hz visual and/or auditory stimuli has been found to help alleviate the amyloid burden from medial prefrontal cortex (Martorell et al., 2019). These reports strongly suggest that temporally structured sensory stimuli can be used as a tool to treat patients with Alzheimer's disease. A recent report indicating that humans can use temporal olfactory cues suggests this may be possible for olfaction as well (Perl et al., 2020). Therefore, temporally structured odor stimuli could offer an additional route for treatment for neurodegenerative disorders.

Overall, in this study we report that M/TCs in the mouse olfactory bulb can encode temporal structure in odor stimuli and that their membrane potentials can follow frequencies of at least up to 20 Hz. Extent of coupling is independent of the odors presented, varies between cells, and is shaped by inhibition in the olfactory bulb.

References

Abraham NM, Egger V, Shimshek DR, Renden R, Fukunaga I, Sprengel R, Seeburg PH, Klugmann M, Margrie TW, Schaefer AT, Kuner T (2010) Synaptic inhibition in the olfactory bulb accelerates odor discrimination in mice. Neuron 65:399–411.

Ackels T, Jordan R, Schaefer AT, Fukunaga I (2020) Respiration-locking of olfactory receptor and projection neurons in the mouse olfactory bulb and its modulation by brain state. Front Cell Neurosci 14:220.

Ackels T, Erskine A, Dasgupta D, Marin AC, Warner TPA, Tootoonian S, Fukunaga I, Harris JJ, Schaefer AT (2021) Fast odor dynamics are encoded in the olfactory system and guide behaviour. Nature 593:558–563.

Atallah BV, Scanziani M (2009) Instantaneous modulation of gamma oscillation frequency by balancing excitation with inhibition. Neuron 62:566–577.

Aungst JL, Heyward PM, Puche AC, Karnup SV, Hayar A, Szabo G, Shipley MT (2003) Centre-surround inhibition among olfactory bulb glomeruli. Nature 426:623–629.

Banerjee A, Marbach F, Anselmi F, Koh MS, Davis MB, Garcia da Silva P, Delevich K, Oyibo HK, Gupta P, Li B, Albeanu DF (2015) An interglomerular circuit gates glomerular output and implements gain control in the mouse olfactory bulb. Neuron 87:193–207.

Benabid AL, Pollak P, Louveau A, Henry S, de Rougemont J (1987) Combined (thalamotomy and stimulation) stereotactic surgery of the VIM thalamic nucleus for bilateral Parkinson disease. Appl Neurophysiol 50:344–346.

Bolding KA, Nagappan S, Han BX, Wang F, Franks KM (2020) Recurrent circuitry is required to stabilize piriform cortex odor representations across brain states. Elife 9:e53125.

Borghuis BG, Tadin D, Lankheet MJM, Lappin JS, van de Grind WA (2019) Temporal limits of visual motion processing: psychophysics and neurophysiology. Vision (Basel) 3:5.

Buracas GT, Zador AM, DeWeese MR, Albright TD (1998) Efficient discrimination of temporal patterns by motion-sensitive neurons in primate visual cortex. Neuron 20:959–969.

Burton SD (2017) Inhibitory circuits of the mammalian main olfactory bulb. J Neurophysiol 118:2034–2051.

Carr CE (1993) Processing of temporal information in the brain. Annu Rev Neurosci 16:223–243.

Celani A, Villermaux E, Vergassola M (2014) Odor landscapes in turbulent environments. Phys Rev X 4:041015.

Chou TH, Toft-Nielsen J, Porciatti V (2019) Adaptation of retinal ganglion cell function during flickering light in the mouse. Sci Rep 9:18396.

Connelly T, Yu Y, Grosmaitre X, Wang J, Santarelli LC, Savigner A, Qiao X, Wang Z, Storm DR, Ma M (2015) G protein-coupled odorant receptors underlie mechanosensitivity in mammalian olfactory sensory neurons. Proc Natl Acad Sci U S A 112:590–595.

Crimaldi J, Lei H, Schaefer A, Schmuker M, Smith BH, True AC, Verhagen JV, Victor JD (2022) Active sensing in a dynamic olfactory world. J Comput Neurosci 50:1–6.

Cury KM, Uchida N (2010) Robust odor coding via inhalation-coupled transient activity in the mammalian olfactory bulb. Neuron 68:570–585.

Deneux T, Kempf A, Daret A, Ponsot E, Bathellier B (2016) Temporal asymmetries in auditory coding and perception reflect multi-layered nonlinearities. Nat Commun 7:12682.

Díaz-Quesada M, Youngstrom IA, Tsuno Y, Hansen KR, Economo MN, Wachowiak M (2018) Inhalation frequency controls reformatting of mitral/tufted cell odor representations in the olfactory bulb. J Neurosci 38:2189–2206.

Eiting TP, Wachowiak M (2020) Differential impacts of repeated sampling on odor representations by genetically-defined mitral and tufted cell subpopulations in the mouse olfactory bulb. J Neurosci 40:6177–6188.

Fackrell JE, Robins AG (1982) Concentration fluctuations and fluxes in plumes from point sources in a turbulent boundary layer. J Fluid Mech 117:1–26.

Fukunaga I, Berning M, Kollo M, Schmaltz A, Schaefer AT (2012) Two distinct channels of olfactory bulb output. Neuron 75:320–329.

Fukunaga I, Herb JT, Kollo M, Boyden ES, Schaefer AT (2014) Independent control of gamma and theta activity by distinct interneuron networks in the olfactory bulb. Nat Neurosci 17:1208–1216.

Ghatpande AS, Reisert J (2011) Olfactory receptor neuron responses coding for rapid odor sampling. J Physiol 589:2261–2273.

Grosmaitre X, Santarelli LC, Tan J, Luo M, Ma M (2007) Dual functions of mammalian olfactory sensory neurons as odor detectors and mechanical sensors. Nat Neurosci 10:348–354.

Gschwend O, Beroud J, Carleton A (2012) Encoding odorant identity by spiking packets of rate-invariant neurons in awake mice. PLoS One 7: e30155.

Gupta P, Albeanu DF, Bhalla US (2015) Olfactory bulb coding of odors, mixtures and sniffs is a linear sum of odor time profiles. Nat Neurosci 18:272–281.

Hendrichs J, Katsoyannos BI, Wornoayporn V, Hendrichs MA (1994) Odor-mediated foraging by yellowjacket wasps (Hymenoptera: Vespidae): predation on leks of pheromone-calling Mediterranean fruit fly males (Diptera: Tephritidae). Oecologia 99:88–94.

Hopfield JJ (1991) Olfactory computation and object perception. Proc Natl Acad Sci U S A 88:6462–6466.

Huston SJ, Stopfer M, Cassenaer S, Aldworth ZN, Laurent G (2015) Neural encoding of odors during active sampling and in turbulent plumes. Neuron 88:403–418.

Jordan R (2021) Optimized protocol for *in vivo* whole-cell recordings in head-fixed, awake behaving mice. STAR Protoc 2:100347.

Jordan R, Fukunaga I, Kollo M, Schaefer AT (2018a) Active sampling state dynamically enhances olfactory bulb odor representation. Neuron 98:1214–1228.e1215.

Jordan R, Kollo M, Schaefer AT (2018b) Sniffing fast: paradoxical effects on odor concentration discrimination at the levels of olfactory bulb output and behavior. eNeuro 5:ENEURO.0148-18.2018.

Kato HK, Chu MW, Isaacson JS, Komiyama T (2012) Dynamic sensory representations in the olfactory bulb: modulation by wakefulness and experience. Neuron 76:962–975.

Kato HK, Gillet SN, Peters AJ, Isaacson JS, Komiyama T (2013) Parvalbumin-expressing interneurons linearly control olfactory bulb output. Neuron 80:1218–1231.

Kauffmann L, Ramanoël S, Peyrin C (2014) The neural bases of spatial frequency processing during scene perception. Front Integr Neurosci 8:37.

Kauffmann L, Bourgin J, Guyader N, Peyrin C (2015) The neural bases of the semantic interference of spatial frequency-based information in scenes. J Cogn Neurosci 27:2394–2405.

Kollo M, Schmaltz A, Abdelhamid M, Fukunaga I, Schaefer AT (2014) "Silent" mitral cells dominate odor responses in the olfactory bulb of awake mice. Nat Neurosci 17:1313–1315.

Laxton AW, Tang-Wai DF, McAndrews MP, Zumsteg D, Wennberg R, Keren R, Wherrett J, Naglie G, Hamani C, Smith GS, Lozano AM (2010) A phase I trial of deep brain stimulation of memory circuits in Alzheimer's disease. Ann Neurol 68:521–534.

Li A, Gire DH, Bozza T, Restrepo D (2014) Precise detection of direct glomerular input duration by the olfactory bulb. J Neurosci 34:16058–16064.

Macrides F, Chorover SL (1972) Olfactory bulb units: activity correlated with inhalation cycles and odor quality. Science 175:84–87.

Margrie TW, Schaefer AT (2003) Theta oscillation coupled spike latencies yield computational vigour in a mammalian sensory system. J Physiol 546:363–374.

Margrie TW, Sakmann B, Urban NN (2001) Action potential propagation in mitral cell lateral dendrites is decremental and controls recurrent and lateral inhibition in the mammalian olfactory bulb. Proc Natl Acad Sci U S A 98:319–324.

Margrie TW, Brecht M, Sakmann B (2002) *In vivo*, low-resistance, whole-cell recordings from neurons in the anaesthetized and awake mammalian brain. Pflugers Arch 444:491–498.

Marin AC, Schaefer AT, Ackels T (2021) Spatial information from the odour environment in mammalian olfaction. Cell Tissue Res 383:473–483.

Martinez D, Moraud EM (2013) Reactive and cognitive search strategies for olfactory robots. In: Neuromorphic olfaction (Persaud KC, Marco S, Gutiérrez-Galvez A, eds). Boca Raton, FL: CRC Press.

Martorell AJ, Paulson AL, Suk HJ, Abdurrob F, Drummond GT, Guan W, Young JZ, Kim DN, Kritskiy O, Barker SJ, Mangena V, Prince SM, Brown EN, Chung K, Boyden ES, Singer AC, Tsai LH (2019) Multi-sensory gamma stimulation ameliorates Alzheimer's-associated pathology and improves cognition. Cell 177:256–271.e222.

Miyamichi K, Shlomai-Fuchs Y, Shu M, Weissbourd BC, Luo L, Mizrahi A (2013) Dissecting local circuits: parvalbumin interneurons underlie broad feedback control of olfactory bulb output. Neuron 80:1232–1245.

Moore PA, Atema J (1991) Spatial information in the three-dimensional fine structure of an aquatic odor plume. Biol Bull 181:408–418.

Mylne KR, Mason PJ (1991) Concentration fluctuation measurements in a dispersing plume at a range of up to 1000 m. Q J Roy Meteor Soc 117:177–206.

Nagayama S, Enerva A, Fletcher ML, Masurkar AV, Igarashi KM, Mori K, Chen WR (2010) Differential axonal projection of mitral and tufted cells in the mouse main olfactory system. Front Neural Circuits 4:120.

Nagel KI, Wilson RI (2011) Biophysical mechanisms underlying olfactory receptor neuron dynamics. Nat Neurosci 14:208–216.

Nagel KI, Hong EJ, Wilson RI (2015) Synaptic and circuit mechanisms promoting broadband transmission of olfactory stimulus dynamics. Nat Neurosci 18:56–65.

Nelken I, Rotman Y, Bar Yosef O (1999) Responses of auditory-cortex neurons to structural features of natural sounds. Nature 397:154–157.

O'Sullivan C, Weible AP, Wehr M (2019) Auditory cortex contributes to discrimination of pure tones. eNeuro 6:ENEURO.0340-19.2019.

Pannunzi M, Nowotny T (2019) Odor stimuli: not just chemical identity. Front Physiol 10:1428.

Parabucki A, Bizer A, Morris G, Munoz AE, Bala ADS, Smear M, Shusterman R (2019) Odor concentration change coding in the olfactory bulb. eNeuro 6:ENEURO.0396-18.2019.

Perl O, Nahum N, Belelovsky K, Haddad R (2020) The contribution of temporal coding to odor coding and odor perception in humans. Elife 9: e49734.

Rebello MR, McTavish TS, Willhite DC, Short SM, Shepherd GM, Verhagen JV (2014) Perception of odors linked to precise timing in the olfactory system. PLoS Biol 12:e1002021.

Reisert J, Matthews HR (2001) Response properties of isolated mouse olfactory receptor cells. J Physiol 530:113–122.

Riffell JA, Abrell L, Hildebrand JG (2008) Physical processes and real-time chemical measurement of the insect olfactory environment. J Chem Ecol 34:837–853.

Rinberg D, Koulakov A, Gelperin A (2006) Sparse odor coding in awake behaving mice. J Neurosci 26:8857–8865.

Schaefer AT, Angelo K, Spors H, Margrie TW (2006) Neuronal oscillations enhance stimulus discrimination by ensuring action potential precision. PLoS Biol 4:e163.

Schmuker M, Bahr V, Huerta R (2016) Exploiting plume structure to decode gas source distance using metal-oxide gas sensors. Sensor Actuat B-Chem 235:636–646.

Schneider SP, Scott JW (1983) Orthodromic response properties of rat olfactory bulb mitral and tufted cells correlate with their projection patterns. J Neurophysiol 50:358–378.

Scott JW, McBride RL, Schneider SP (1980) The organization of projections from the olfactory bulb to the piriform cortex and olfactory tubercle in the rat. J Comp Neurol 194:519–534.

Sehdev A, Mohammed YG, Triphan T, Szyszka P (2019) Olfactory object recognition based on fine-scale stimulus timing in *Drosophila*. iScience 13:113–124.

Short SM, Wachowiak M (2019) Temporal dynamics of inhalation-linked activity across defined subpopulations of mouse olfactory bulb neurons imaged *in vivo*. eNeuro 6:ENEURO.0189-19.2019.

Shraiman BI, Siggia ED ED (2000) Scalar turbulence. Nature 405:639–646.

Shusterman R, Smear MC, Koulakov AA, Rinberg D (2011) Precise olfactory responses tile the sniff cycle. Nat Neurosci 14:1039–1044.

Sicard G (1986) Electrophysiological recordings from olfactory receptor cells in adult mice. Brain Res 397:405–408.

Smear M, Shusterman R, O'Connor R, Bozza T, Rinberg D (2011) Perception of sniff phase in mouse olfaction. Nature 479:397–400.

Szyszka P, Stierle JS, Biergans S, Galizia CG (2012) The speed of smell: odor-object segregation within milliseconds. PLoS One 7:e36096.

Szyszka P, Gerkin RC, Galizia CG, Smith BH (2014) High-speed odor transduction and pulse tracking by insect olfactory receptor neurons. Proc Natl Acad Sci U S A 111:16925–16930.

Theunissen FE, Elie JE (2014) Neural processing of natural sounds. Nat Rev Neurosci 15:355–366.

Tramo MJ, Shah GD, Braida LD (2002) Functional role of auditory cortex in frequency processing and pitch perception. J Neurophysiol 87:122–139.

VanRullen R, Zoefel B, Ilhan B (2014) On the cyclic nature of perception in vision versus audition. Philos Trans R Soc Lond B Biol Sci 369:20130214.

Vergassola M, Villermaux E, Shraiman BI (2007) "Infotaxis" as a strategy for searching without gradients. Nature 445:406–409.

Verhagen JV, Wesson DW, Netoff TI, White JA, Wachowiak M (2007) Sniffing controls an adaptive filter of sensory input to the olfactory bulb. Nat Neurosci 10:631–639.

Vickers NJ, Baker TC (1994) Reiterative responses to single strands of odor promote sustained upwind flight and odor source location by moths. Proc Natl Acad Sci U S A 91:5756–5760.

Vickers NJ, Christensen TA, Baker TC, Hildebrand JG (2001) Odor-plume dynamics influence the brain's olfactory code. Nature 410:466–470.

Wang HP, Garcia JW, Sabottke CF, Spencer DJ, Sejnowski TJ (2019) Feedforward thalamocortical connectivity preserves stimulus timing information in sensory pathways. J Neurosci 39:7674–7688.

Yokoi M, Mori K, Nakanishi S (1995) Refinement of odor molecule tuning by dendrodendritic synaptic inhibition in the olfactory bulb. Proc Natl Acad Sci U S A 92:3371–3375.

Zeppilli S, Ackels T, Attey R, Klimpert N, Ritola KD, Boeing S, Crombach A, Schaefer AT, Fleischmann A (2021) Molecular characterization of projection neuron subtypes in the mouse olfactory bulb. Elife 10:e65445.

Zhang C, Pan Y, Zhou H, Xie Q, Sun B, Niu CM, Li D (2019) Variable high-frequency deep brain stimulation of the subthalamic nucleus for speech disorders in Parkinson's disease: a case report. Front Neurol 10:379.